Sexually dimorphic RNA helicases DDX3X and DDX3Y differentially regulate RNA metabolism through phase separation

Hui Shen[1,7], Amber Yanas[1,2,7], Michael C. Owens[1,2], Celia Zhang[1], Clark Fritsch[3], Charlotte M. Fare[1,2], Katie E. Copley[1,4], James Shorter[1,2], Yale E. Goldman[2,5,6], Kathy Fange Liu[1,2,8,*]

[1]Department of Biochemistry and Biophysics, Perelman School of Medicine, University of Pennsylvania, Philadelphia, PA 19104, USA

[2]Graduate Group in Biochemistry and Molecular Biophysics, Perelman School of Medicine, University of Pennsylvania, Philadelphia, PA 19104, USA

[3]Graduate Group in Cellular and Molecular Biology, Perelman School of Medicine, University of Pennsylvania, Philadelphia, PA 19104, USA

[4]Graduate Group in Neuroscience, Perelman School of Medicine, University of Pennsylvania, Philadelphia, PA 19104, USA

[5]Department of Physiology, Perelman School of Medicine, University of Pennsylvania, Philadelphia, PA 19104, USA

[6]Pennsylvania Muscle Institute, Perelman School of Medicine, University of Pennsylvania, Philadelphia, PA 19104, USA

[7]These authors contributed equally

[8]Lead contact

SUMMARY

Sex differences are pervasive in human health and disease. One major key to sex-biased differences lies in the sex chromosomes. Although the functions of the X-chromosome proteins are well appreciated, how they compare with their Y-chromosome homologs remains elusive. Herein, using ensemble and single-molecule techniques, we report that the sex chromosome-

Author Manuscript

encoded RNA helicases DDX3X and DDX3Y are distinct in their propensities for liquid-liquid phase separation (LLPS), dissolution, and translation repression. We demonstrate that the N-terminal intrinsically disordered region of DDX3Y more strongly promotes LLPS than the corresponding region of DDX3X and that the weaker ATPase activity of DDX3Y compared to DDX3X contributes to the slower disassembly dynamics of DDX3Y-positive condensates. Interestingly, DDX3Y-dependent LLPS represses mRNA translation and enhances aggregation of FUS more strongly than DDX3X-dependent LLPS. Our study provides a platform for future comparisons of sex chromosome-encoded protein homologs, providing insights into sex differences in RNA metabolism and human disease.

eTOC Blurb:

Shen et al. report that the Y chromosome-encoded RNA helicase DDX3Y has stronger propensity for liquid-liquid phase separation compared to its X chromosome-encoded homolog DDX3X, which results in the stronger repression of mRNA translation and promotion of FUS aggregation under stress conditions.

Graphical Abstract
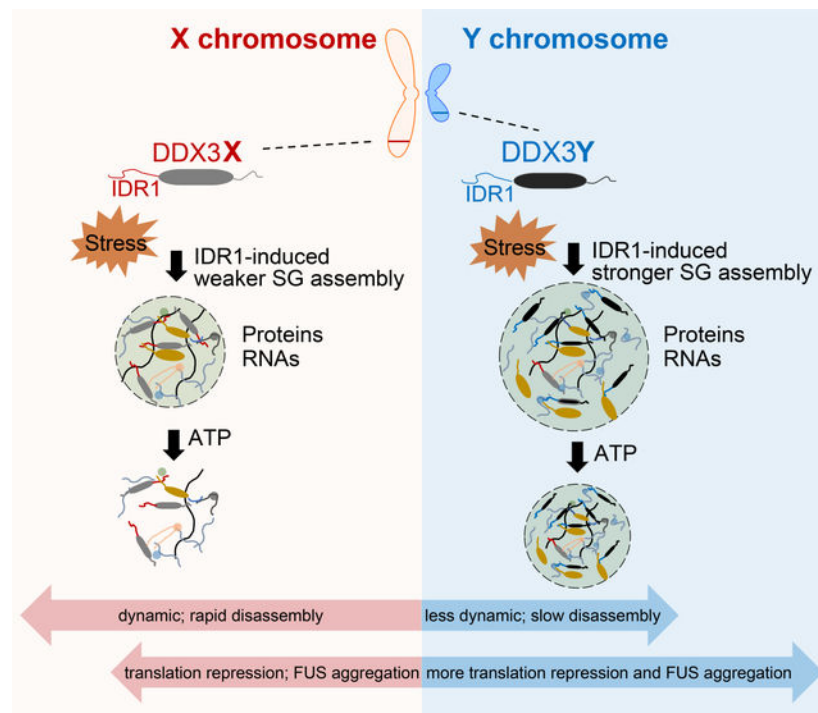
Keywords

Sex chromosome homolog proteins; DDX3X; DDX3Y; RNA helicase; liquid-liquid phase separation; condensates; ATPase activity; translation repression

INTRODUCTION

Many human disorders manifest in a sex-biased manner, yet the molecular mechanisms responsible for these biases are not fully understood (Mauvais-Jarvis et al., 2020). On a genetic level, the most significant differences between males and females lie in the sex chromosomes. Although the X and Y chromosomes are, by and large, not homologous, a handful of X chromosome-encoded proteins have Y chromosome-encoded homologs (Bellott et al., 2014). These Y chromosome-encoded homologs were historically thought to only be expressed and to function in the reproductive system. However, a growing body of evidence suggests that Y chromosome-encoded homologs are not only expressed throughout the body at the transcript and protein levels but are also evolutionarily conserved (Godfrey et al., 2020). However, the functional differences between the protein homologs encoded on the X and Y chromosomes have not been thoroughly investigated. Emerging evidence is starting to reveal that Y chromosome-encoded proteins may function differently from their X chromosome-encoded homologs (Gozdecka et al., 2018; Nguyen et al., 2020; Shi et al., 2021).

One pair of sex chromosome-encoded proteins are the RNA helicases DDX3X and DDX3Y. In females (specified as XX individuals), DDX3X escapes X-inactivation, and two copies of the protein are expressed, whereas in males (specified as XY individuals), one copy of each of the X- and Y-linked proteins is expressed (Cotton et al., 2015; Ditton et al., 2004). The *DDX3X* gene (Xp11.4) encodes a DEAD-box RNA helicase (Sharma and Jankowsky, 2014), which is evolutionarily conserved in *C. elegans* (LAF-1), yeast (Ded1p), *Drosophila* (Belle), and humans (Sharma and Jankowsky, 2014). The functions of DDX3X are more well studied than those of DDX3Y, and include its activity as a translation-initiation factor (Lai et al., 2008; Lee et al., 2008) for a set of mRNAs with highly structured 5'-UTRs (Ku et al., 2019; Lai et al., 2008; Lee et al., 2008; Phung et al., 2019; Soto-Rifo et al., 2012), and at repeat-associated non-AUG (RAN) start sites (Cheng et al., 2019; Linsalata et al., 2019). In addition, DDX3X (and its homologs) undergoes liquid-liquid phase separation (LLPS) and is a conserved component of stress granules (SGs) (Beckham et al., 2008; Elbaum-Garfinkle et al., 2015; Iserman et al., 2020; Shih et al., 2012; Valentin-Vega et al., 2016). SGs, which are composed of RNAs and proteins and form as part of the stress response, are correlated with changes to mRNA metabolism, including translational repression (Kimball et al., 2003; Moon et al., 2019). Dysregulation of SGs has been implicated in a wide range of human disorders, including cardiomyopathy, Alzheimer's disease, and amyotrophic lateral sclerosis (ALS), many of which present with a varying degree of sex-biased incidences, progressions, and outcomes (Ash et al., 2014; Baradaran-Heravi et al., 2020; Ferretti et al., 2018; Manjaly et al., 2010; McCombe and Henderson, 2010; Meyer et al., 2014; Schneider et al., 2020; Watkins et al., 2020). Additionally, DDX3X mutations can lead to DDX3X syndrome, a disorder which accounts for 1–3% of intellectual disability cases and is more prevalent in females than in males (Iossifov et al., 2014; Lennox et al., 2020; Ruzzo et al., 2019; Scala et al., 2019; Snijders Blok et al., 2015; Wang et al., 2018b).

Notably, the presence of the *DDX3Y* gene can only sometimes compensate for the loss of the *DDX3X* gene (Chen et al., 2016). For example, *Ddx3y* cannot fully compensate for the loss of *Ddx3x* during embryonic and neuronal development in mice (Chen et al., 2016;

Patmore et al., 2020). Furthermore, male mice, but not female mice, survive conditional knockout of *Ddx3x* in the bone marrow, but these male mice present with distinct deficiencies in innate antimicrobial immunity compared to *Ddx3x* conditional knockout female mice (Szappanos et al., 2018). These findings highlight the fact that DDX3X and DDX3Y have roles beyond the reproductive system and suggest that *Ddx3x* and *Ddx3y* possibly have distinct functions in immune cells (Szappanos et al., 2018). Indeed, recently compiled proteomic databases show that both DDX3X and DDX3Y proteins are expressed in the human immune system, including in T-cells, B-cells, and NK-cells (Bryk and Wisniewski, 2017; Joshi et al., 2019). Moreover, previous studies revealed that the DDX3Y protein is present in the enteric nervous system and the human heart (Cardinal et al., 2020; Godfrey et al., 2020; Vakilian et al., 2015). Still, potential functional differences between DDX3X and DDX3Y and their contributions to sex-biased human diseases are largely unknown.

Like other DEAD-box helicases, DDX3X and DDX3Y contain a helicase core composed of two RecA-like domains and one intrinsically disordered region (IDR) on each of the N- and C-termini. IDRs are frequently involved in the process of LLPS, driven by weak multivalent interactions (Figure 1A). Although DDX3X and DDX3Y share 92% amino acid sequence identity overall, the N-terminal IDRs (IDR1) are more divergent, accounting for 60% difference between DDX3X and DDX3Y (Figure S1A and S1B). IDR1 of DDX3X specifically is known to be essential for its LLPS *in vitro* and inside cells (Saito et al., 2019; Shih et al., 2012). Since many of the differences between the sequences of DDX3X and DDX3Y are concentrated in IDR1, we wondered whether DDX3X and DDX3Y differ in their propensity to LLPS and consequently differ in responding to cellular stress.

Here, we show that DDX3Y has a greater LLPS propensity than DDX3X. DDX3Y-positive SGs are less dynamic (less able to exchange particles with the light phase) than DDX3X-positive SGs. Furthermore, we demonstrate that while DDX3X-positive and DDX3Y-positive SGs share a large overlap of RNA constituents, there are also RNA components that are unique to either SG. We also show that the condensation of either DDX3X or DDX3Y represses the translation of RNAs, with DDX3Y condensation showing a significantly stronger inhibitory effect. Additionally, we show that both helicases specifically augment the aggregation of FUS *in vitro* and in cells, with DDX3Y having a more profound effect. Collectively, our results suggest that these sexually dimorphic RNA helicases differentially regulate RNA metabolism through their distinct biochemical and biophysical properties, which might contribute to sex bias in human diseases.

RESULTS

DDX3Y has a stronger propensity than DDX3X for *in vitro* and cellular phase separation

Given that DDX3X is known to undergo LLPS *in vitro,* we wanted to establish whether DDX3Y could also phase separate, and how it is compared to DDX3X. Thus, we purified mCherry-tagged full-length DDX3X and DDX3Y to near homogeneity (Figure S1C and S1D). Full-length mCherry-tagged DDX3X and DDX3Y formed noticeable droplets *in vitro*, and the addition of poly(U)-RNA greatly stimulated this process (Figure 1B and 1C). Strikingly, DDX3Y phase separation was more strongly enhanced by the addition

of poly(U)-RNA than DDX3X *in vitro*; the average integrated fluorescence intensity of DDX3Y droplets was ~10-fold higher than an equal amount of DDX3X (Figure 1B and 1C). As shown in Figure S1E, RNase treatment had no influence on the *in vitro* droplet formation, indicating negligible RNA carry-over during protein purification. Furthermore, we determined the saturation concentration (C_{sat}) of DDX3X and DDX3Y using sedimentation analysis. The C_{sat} of DDX3X was ~5 μM whereas DDX3Y was ~3 μM, indicating that DDX3Y undergoes LLPS at lower concentrations than DDX3X (Figure 1D). In parallel, we performed a turbidity assay; the results consistently showed that DDX3Y gave substantially higher turbidity at the same total protein concentrations compared to DDX3X (Figure 1E), suggesting a greater degree of phase separation.

We next studied the dynamics of DDX3X and DDX3Y droplets using fluorescent recovery after photobleaching (FRAP). The recovery halftime for DDX3X droplets was ~21.9 seconds, which was significantly faster than the ~83.4 seconds for DDX3Y droplets (Figures 1F, 1G, S1F, and Movies S1 – S4). Also, we observed a larger mobile fraction for DDX3X droplets (~99%) than for DDX3Y droplets (~78%) (Figure 1H). These results demonstrate that DDX3X is less prone to phase separation and that DDX3X droplets are more dynamic than DDX3Y droplets *in vitro*.

To assess if DDX3Y enters cellular SGs, we expressed DDX3X or DDX3Y in several mammalian cell types, each of which lacks endogenous DDX3Y (HeLa, N2a, and HEK 293T cells). Before expressing either protein, we performed a transient knockdown of endogenous DDX3X with >80% knockdown efficiency (Figure S2A). Exogenous expressions of DDX3X and DDX3Y were at a similar level (Figure S2B and S2C). DDX3X and DDX3Y were diffuse throughout the cytoplasm in unstressed HeLa cells (Figure S2D). Upon arsenite treatment (a commonly used oxidative-stress inducer (Markmiller et al., 2018; Protter and Parker, 2016)), both DDX3X and DDX3Y colocalized with the stress granule marker, G3BP1 (Markmiller et al., 2018) (Figure 2A). Strikingly, the total area of DDX3Y-positive SGs was larger than DDX3X-positive SGs in HeLa cells (1.6-fold), N2a cells (1.3-fold), and HEK293T cells (1.7-fold) (Figure 2B). To control for possible differences in protein concentrations, we expressed DDX3X and DDX3Y across a range of concentrations in HeLa cells with endogenous DDX3X depleted. The results consistently showed that DDX3Y-positive granules were significantly larger than DDX3X-positive granules at similar expressed concentrations (Figure S2E – S2G). Additionally, we quantified the protein half-life of DDX3X and DDX3Y in HeLa cells using cycloheximide (CHX) chase experiments. As shown in Figure 2C and 2D, the cellular half-life of DDX3X is indistinguishable from DDX3Y. FRAP experiments performed on live HeLa cells expressing DDX3X-EGFP or DDX3Y-EGFP (Figure S2H) reveal that the average recovery halftime of DDX3X-positive granules was ~7.6 s, which was significantly faster than the ~10.2 s measured for DDX3Y-positive SGs (Figure 2E – 2G, Movies S5 and S6). Additionally, a larger mobile fraction was observed in DDX3X-positive SGs (86%) than in DDX3Y-positive SGs (77%) (Figure 2G), consistent with our *in vitro* FRAP experiments. These results together suggest that DDX3X-positive SGs are more dynamic than DDX3Y-positive SGs.

IDR1 is a major contributor to the higher phase separation propensity of DDX3Y

We constructed several truncated variants of DDX3X and DDX3Y to study the effect of each domain on SG partitioning (Figure S3A and S3B). Deletion of IDR1 from DDX3X (DDX3X $^{\Delta IDR1}$) and DDX3Y (DDX3Y $^{\Delta IDR1}$) led to the sequestration of the variants into cell nuclei and thus completely prevented either protein from entering cytoplasmic SGs, which is consistent with previous work showing that IDR1 of DDX3X contains a nuclear export sequence (Yedavalli et al., 2004) (Figures S1A and S3C). Both DDX3X $^{\Delta IDR1}$ and DDX3Y $^{\Delta IDR1}$ were diffuse in the nucleus, even with arsenite treatment (Figure S3C), so we hypothesized that the high nuclear RNA concentrations prevented these truncations from forming condensates, since this phenomenon has been seen with other RNA-binding proteins with IDRs (Maharana et al., 2018). To test this, we treated cells expressing DDX3X $^{\Delta IDR1}$ or DDX3Y $^{\Delta IDR1}$ with actinomycin D (ActD), which inhibits transcription and thus decreases RNA levels. ActD treatment led to the formation of DDX3X and DDX3Y puncta inside the nucleus, consistent with an RNA-dependent LLPS buffering mechanism (Figure S3D).

Deleting any individual domain in DDX3X and DDX3Y dramatically decreased SG area compared to the full-length (Figures 3A, 3B, S3A, and S3B). Consistent with previous results, IDR1 of either DDX3X or DDX3Y as a standalone protein entered SGs and colocalized with G3BP1. Furthermore, a noticeable fraction of IDR1 from either protein remained diffuse throughout the cytoplasm upon arsenite treatment, indicating that IDR1 alone is less prone to enter SGs. For DDX3X, the deletion of IDR2 (DDX3X $^{\Delta IDR2}$) significantly decreased the total SG area of DDX3X $^{\Delta IDR2}$-positive SGs per cell (by ~1.4 fold) compared to the wild-type-DDX3X SGs. Deletion of the helicase domains (both DEAD1 and DEAD2) from DDX3X also decreased the total area of DDX3X $^{\Delta helicase}$-SGs (~1.2 fold) per cell, but to a lesser extent than the deletion of IDR1 or IDR2. Similarly, for DDX3Y, deletion of IDR2 or the helicase domains both lead to a ~1.2-fold decrease in the size of DDX3Y $^{\Delta IDR2}$-positive or DDX3Y $^{\Delta helicase}$-positive SGs compared to the full-length DDX3Y SGs. Notably, the total SG area for each DDX3Y truncation was still larger than their DDX3X truncation counterparts (~1.3 to 1.85-fold), suggesting that subtle sequence variation throughout the protein contributes to the distinct behaviors of DDX3X and DDX3Y (Figure 3A and 3B).

When we swapped IDRs between DDX3X and DDX3Y, we observed that any domain-swapped variants containing IDR1 of DDX3Y formed significantly larger SGs than the hybrid variants that did not contain IDR1 of DDX3Y, whereas swapping helicase domains or IDR2 did not significantly affect SG sizes (Figures 3C, 3D, S3E, and S3F). When we performed *in vitro* droplet formation assays with wild-type and domain-swapped variants (which were purified to a similar level of homogeneity, Figure S3G and S3H), our results recapitulated the finding that any domain-swapped variants that contained IDR1 of DDX3Y more readily phase-separated in the presence of RNA than variants which did not contain IDR1 of DDX3Y (Figure 3E and 3F). Our results also suggest that the IDR2 and helicase domains may also contribute to the differences in propensity to undergo LLPS, as the $X^{IDR1}Y^{helicase}Y^{IDR2}$ variant more readily formed droplets compared to wild-type DDX3X, $X^{IDR1}Y^{helicase}X^{IDR2}$, and $X^{IDR1}X^{helicase}Y^{IDR2}$ (Figure 3D and 3F). To dissect

the contributions of RNA binding and IDRs in phase separation of the proteins, we next performed the *in vitro* droplet assays with wild-type and domain-swapped variants in the absence of poly(U)-RNA. As shown in Figure S3I, proteins containing IDR1 of DDX3Y formed larger droplets than proteins containing IDR1 of DDX3X. These results suggest that although each of the domains in DDX3 proteins plays a distinct role in facilitating LLPS and in their accumulation into SGs, the sequence of IDR1 is a significant factor in determining the relative droplet sizes.

The weaker ATPase activity of DDX3Y compared to DDX3X weakens its condensate disassembly

DDX3X and DDX3Y harness the energy of ATP hydrolysis to control RNA binding, unwinding, and release (Hondele et al., 2019). Because LLPS droplets assemble through many multivalent, weak interactions between RNAs and proteins (Wang et al., 2018a), we stimulated the ATPase activity of DDX3X and DDX3Y to see if this could induce condensation disassembly by affecting RNA-protein interactions. As shown in Figure 4A and 4B, the addition of 4 mM ATP to protein-RNA droplets induced the disassembly of both DDX3X and DDX3Y condensates. To control for the hydrotropic effect of ATP (Patel et al., 2017) in dissolving the droplets, we repeated the droplet assay using UTP (which is not hydrolyzed by DDX3 and thus could only act as a hydrotrope in this context (Patel et al., 2017)). The addition of UTP had no significant effect on the droplets formed by DDX3X and DDX3Y with RNA (Figure 4A and 4B). These results suggest that the ATPase activity of DDX3X and DDX3Y is a major factor in dissolving DDX3-RNA condensation, possibly by breaking the multivalent protein-RNA interactions.

We next studied whether there are intrinsic differences in ATPase activity between DDX3X and DDX3Y, as this could explain the differences observed in their condensate disassembly in response to ATP. Thus, we measured the ATPase activities of both DDX3X and DDX3Y using a malachite green ATPase assay. In this assay, we used MBP-tagged proteins purified to near homogeneity (Figure S4A and S4B). Both of the MBP-tagged DDX3X and DDX3Y displayed the same melting temperatures in differential scanning fluorimetry measurements, and the melting curves are indicative of well-folded proteins devoid of aggregates (Figure S4C and S4D) (Gao et al., 2020).

To ensure that any potential RNA carry-over would not confound our measurements, we performed the malachite green ATPase assays in the absence of additional RNA or with 100 ng/μL total HeLa RNA. In reactions with no added RNA but with 2 mM ATP, DDX3X and DDX3Y reactions had nearly identical amounts of free phosphate after a 30-minute reaction time (Figure S4E). This phosphate is likely due to spontaneous hydrolysis of ATP, as it is also present in the controls with buffer only. When RNA was added, DDX3X reactions produced more free phosphates (indicative of more ATP hydrolysis) than DDX3Y reactions. The malachite green ATPase assays were also performed using RNase treated and untreated MBP-tagged DDX3X and DDX3Y respectively. As shown in Figure S4F, RNase treatment has no noticeable effects on the ATPase activities. Collectively, these results suggest that DDX3X is a more robust ATPase than DDX3Y, and that the possible trace amount of RNA

carry-over in the purified MBP-tagged DDX3X and DDX3Y was not responsible for the ATPase activity differences.

To obtain a more complete picture of the ATPase differences between DDX3X and DDX3Y, we performed a continuous ATPase assay as previously reported using the MBP-tagged DDX3X and DDX3Y constructs (Song and Ji, 2019). DDX3X reached a V_{max} of 7.9 μM/min while DDX3Y only achieved a V_{max} of 5.9 μM/min (Figure 4C). Both DDX3X and DDX3Y hydrolyzed ATP cooperatively (Hill coefficient ≈ 2), as has been previously reported for DDX3X (Song and Ji, 2019). While the ATPase activity of DDX3Y has not been previously investigated, our V_{max} values for the full-length DDX3X were higher than those reported for a truncation lacking both IDRs (amino acids 132 – 607) (7.9 *vs.* 3.1 μM/min, 2.54-fold higher) (Song and Ji, 2019). Our data suggest that ATP hydrolysis activity of DDX3Y is significantly slower than that of DDX3X (Figure 4C).

DDX3X is a non-processive helicase: it binds its dsRNA substrate, binds ATP, unwinds approximately 13 – 19 bp of dsRNA, and releases the two RNA strands upon ATP hydrolysis (Song and Ji, 2019). Given that ATP hydrolysis is a crucial step in this catalytic cycle and that our ATPase data suggest that DDX3X is a more efficient ATPase than DDX3Y, we next investigated how the differences in ATPase activities may affect the dynamics of these enzymes. To this end, we employed smFRET assays with MBP-DDX3X and MBP-DDX3Y to compare their RNA binding abilities and the dynamics of their ATP-dependent interactions with RNA as described previously (Figure 4D) (Kim and Myong, 2016). At protein concentrations of 2, 4, or 8 μM, DDX3X and DDX3Y tightly bound the RNA substrate, resulting in high FRET, with a peak FRET efficiency (*E*) of 0.81 – 0.85 (Figures 4E, S4G, and Table S1). This binding is specific to DDX3X and DDX3Y, as MBP (a non-RNA interacting protein) gave low FRET, like RNA alone (Figure S4H and S4I).

The addition of ATP to DDX3X and DDX3Y led to a low FRET population that was larger for DDX3X than it was for DDX3Y (Figures 4E, S4J, S4K, and Table S1). Of note, this low-FRET population of RNA molecules does not represent full strand separation of the RNA duplex because alternating direct illumination of the Cy3 and Alexa Fluor 647 probes (lowest traces in Figure S4J and S4K) showed that both labeled strands are present in each individual high- and low-FRET particles. This change in FRET from high to low efficiency likely represents partial unwinding activity. As shown in Figure 4F, the relative areas of the low FRET peak induced by addition of ATP increased along with increasing protein concentrations which exemplifies the cooperativity of the DDX3X- and DDX3Y-catalyzed reactions. Importantly, the smFRET histograms suggest that DDX3X had higher (partial) unwinding activity than DDX3Y, consistent with the kinetics data (Figure 4C). DDX3X also showed a larger proportion of dynamic FRET recordings upon addition of ATP than DDX3Y (Figure S4L). Together, the kinetics and smFRET data support the conclusion that DDX3Y has slower ATPase and (partial) unwinding activities, leading to the less dynamic characteristics of RNA-DDX3Y complexes. Decreased dynamics may contribute to the weaker disassembly of DDX3Y condensates compared to those of DDX3X, which in turn contributes to the observation that DDX3Y condensates persist in the presence of ATP to a greater degree than DDX3X condensates (Figure 4A).

Translation is differentially modulated by DDX3X and DDX3Y

Given that SGs are formed concomitant with translational repression and are thought to harbor proteins that regulate translation (Kimball et al., 2003), we employed a reticulocyte *in vitro* translation assay to investigate how phase-separated DDX3X and DDX3Y influence the translation of a luciferase reporter (Figure 5A). Upon titration of 4 – 10 μM mCherry-DDX3X or mCherry-DDX3Y into the lysate, there was a dramatic, dose-dependent decrease of luciferase signal with increased concentrations of DDX3X or DDX3Y, indicating a decrease in the *in vitro* translation (Figure 5B). Indeed, we observed a concentration-dependent increase in protein condensation of DDX3X or DDX3Y within the lysate (Figure 5C and 5D). These results indicate that the condensation of DDX3X and DDX3Y is correlated with repressed mRNA translation. Of note, at each concentration tested, DDX3Y induced a more pronounced decrease in luciferase signal compared to DDX3X (Figure 5B). To ensure that the observed effects were specific to DDX3X and DDX3Y, we also titrated truncated versions of DDX3X and DDX3Y, which only contained the minimally active helicase domain (both RecA-like domains and the N- and C-terminal extensions) (Floor et al., 2016; Song and Ji, 2019) to serve as negative controls. As shown in Figure S5A, the luciferase signal remained steady across all concentrations of the truncated versions of DDX3X and DDX3Y, likely because these constructs lack IDRs. We next studied whether adding ATP could alleviate translation repression by disassembling the DDX3X and DDX3Y condensates in the *in vitro* translation assays. To this end, the assays were repeated with the addition of 1 mM ATP. Upon ATP addition, *in vitro* translation was partially restored in both DDX3X and DDX3Y reactions; however, DDX3Y reactions remained less translationally active than the corresponding DDX3X reactions (Figure S5B). These findings support the notion that the decreased ATPase activity of DDX3Y decelerates the dispersal of DDX3Y-containing condensates, and thus ATP does not fully restore *in vitro* translation.

Next, we investigated whether DDX3Y condensation had a stronger translation repression impact than DDX3Y condensation in cells using a puromycin incorporation assay in HeLa cells after transient transfection of FLAG-DDX3X or FLAG-DDX3Y with endogenous DDX3X depleted. Puromycin was incorporated into newly synthesized proteins, and, as shown in Figure 5E and 5F, the formation of DDX3X-positive SGs and DDX3Y-positive SGs significantly reduced puromycin signals compared to the neighboring cells which were not transfected and thus lacked DDX3X-positive or DDX3Y-positive SGs. Notably, the puromycin signals were weaker in cells with DDX3Y-positive SGs than in cells with DDX3X-positive SGs (Figure 5F). These results suggest a potential mechanism by which DDX3Y more effectively inhibit translation through its unique biophysical properties. Phase separation can inhibit translation by sequestering translational machinery and/or mRNA transcripts into the phase-separated compartment (Kim et al., 2019). DDX3Y-containing condensates and SGs are larger and less mobile (Figures 1 and 2), which may result in stronger translation inhibition than the smaller and more dynamic DDX3X condensates which exchange material more rapidly.

APEX-seq captures the protein-RNA interaction patterns of DDX3X and DDX3Y

SGs formed under different stress conditions contain distinct proteins and RNA constituents (Markmiller et al., 2018), which raises the possibility that SG contents vary based on the

type of stress presented to a cell. Neither the RNA composition nor the differential effects DDX3X or DDX3Y may exert on resident SG RNAs is known. Because SGs are largely thought to be a mechanism of regulating mRNA metabolism (Buchan and Parker, 2009; Jain et al., 2016; Khong et al., 2017), we sought to define the RNA content of DDX3X- and DDX3Y-positive SGs.

To this end, we employed an adapted ascorbate-peroxidase (APEX2)-based proximity labeling method (Fazal et al., 2019; Marmor-Kollet et al., 2020; Padron et al., 2019) (Figure S5C). First, to examine the specificity of APEX2-catalyzed RNA biotinylation, we generated a mito-APEX2 fusion protein consisting of APEX2 fused to a mitochondrial matrix localization signal (Figure S5D) (Fazal et al., 2019; Mercer et al., 2011). Using a previously described protocol (Fazal et al., 2019), followed by RT-qPCR analysis, we could reliably identify mitochondrial-specific RNAs (ND1 and ND2) labeled by mito-APEX2 (Figure S5E – S5G).

Next, using this validated approach, we expressed APEX2-DDX3X, APEX2-DDX3Y, or APEX2-EGFP (control) in DDX3X knockdown HeLa cells. Cells were then treated with arsenite or DMSO for 1 hr to generate three experimental cell populations. We consistently observed that the total area of APEX2-DDX3Y-positive SGs was significantly larger (1.5-fold) than APEX2-DDX3X-positive SGs (Figure S5H and S5I). The results suggest that the fusion of APEX2 to DDX3X or DDX3Y did not significantly interfere with the ability of either protein to colocalize with SGs in cells upon arsenite treatment.

The above cells were then incubated with biotin-phenol for 30 min, followed by H_2O_2 treatment for 1 min to activate the APEX2 enzyme and covalently link biotin to RNAs (Figure 5G). To confirm biotinylating, small aliquots of cell lysate for each condition were blotted using a streptavidin antibody; this antibody detected multiple protein bands (consistent with the previous results (Fazal et al., 2019)), confirming that the APEX2 enzyme was active (Figure S5J and S5K). Subsequently, we performed biotin pulldown and poly(dT) extraction to enrich biotinylated poly(A)-RNAs. Enriched RNAs were subjected to next-generation high-throughput RNA-seq. The RNA-seq data from the biological replicates in each group correlated well (Figure S5L).

To determine whether DDX3X- and DDX3Y-positive SGs harbor unique mRNAs, we compared the levels of transcripts between APEX2-DDX3X or APEX2-DDX3Y libraries to APEX2-EGFP libraries. Any transcript for which expression in either the APEX2-DDX3X or APEX2-DDX3Y libraries was at least 2-fold higher than in the APEX2-EGFP dataset (log_2 -fold enrichment > 1) was defined as "enriched." We found that DDX3X-positive SGs enriched 562 RNAs (Figure 5H and Table S2), and Gene Ontology (GO) analysis indicated the encoded proteins were mainly involved in the regulation of glycolipid and nucleic acid metabolism (Figure 5I). DDX3Y-positive SGs enriched 1020 RNAs (Figure 5H); GO analysis suggested that some of the encoded proteins were also involved in the regulation of glycolipid metabolism, while others play roles in transcriptional regulation (Figure 5I). Interestingly, while there was a large pool of RNAs enriched in both DDX3X- and DDX3Y-positive SGs (where 61% of DDX3X- and 34% of DDX3Y-positive SG enriched RNAs are shared), there are also RNA targets that were specific to each helicase (Figure 5J). In

the absence of arsenite treatment, there was a small number of transcripts with fold change $\log_2 > 1$ or $\log_2 < -1$ in APEX2-DDX3X or APEX2-DDX3Y compared to APEX2-EGFP (Figure S5H and S5M). We validated a list of RNA targets specifically enriched by either APEX2-DDX3X or APEX2-DDX3Y, ranging from lower to upper enrichment, using RT-qPCR (Figure 5K). These results indicate that DDX3X- and DDX3Y-positive SGs regulate distinct mRNA targets. However, DDX3X and DDX3Y may act on shared transcripts in divergent ways as these two enzymes inhibit translation to different degrees (Figure 5A – 5F).

DDX3X and DDX3Y co-phase separate into SGs

While our study up to this point has focused on either DDX3X or DDX3Y individually, XY individuals express both proteins simultaneously (Cotton et al., 2015; Ditton et al., 2004; Godfrey et al., 2020). To examine whether DDX3X and DDX3Y go into the same SGs, we expressed DDX3X and DDX3Y together in cells with endogenous DDX3X transiently knocked down. We found that all the antibodies we tested were highly cross-reactive (Figure S6A), likely due to the high similarity of these two proteins. Thus, we used proteins with different tags (FLAG *vs.* HA), and tagged homologs were expressed to a similar extent (Figure S6B).

Given that SG size and composition are sensitive to different types of stressors (Fujimura et al., 2012; Markmiller et al., 2018; Saito et al., 2019; Szaflarski et al., 2016), we studied SGs triggered by a range of stressors, including energy depletion (CCCP), osmotic stress (sorbitol), translation inhibition (puromycin), proteasome inhibition (MG132), and ER stress (thapsigargin). Under these conditions, MG132 and thapsigargin did not induce SG formation (Figure S6C). However, when CCCP, sorbitol, or puromycin were used to stress cells, DDX3X, DDX3Y, and G3BP1 colocalize, although the fluorescence intensity of FLAG-DDX3X was much lower than HA-DDX3Y (Figure 6A). To ensure that our observations were not due to differential recognition by the anti-FLAG and anti-HA antibodies, we repeated the experiments using HA-DDX3X and FLAG-DDX3Y. We observed the same lower intensity of DDX3X, even though total protein levels for each DDX3 homolog were similar and were not affected by either tag (Figures S6D). These results suggest that, while DDX3X and DDX3Y phase separate to SGs together, DDX3Y has a stronger propensity to go into SGs than DDX3X, in line with our previous observations.

Given that DDX3X and DDX3Y can co-phase separate into SGs, we wondered how mixtures of DDX3X and DDX3Y affected translation compared to DDX3X or DDX3Y alone. As shown in Figure 6B, a 3:1 ratio of DDX3X (6 μM) and DDX3Y (2 μM), which is close to the physiological ratios between DDX3X and DDX3Y (Godfrey et al., 2020), led to a 1.4-fold more robust repression of translation compared to DDX3X (8 μM) alone, and a 3.6-fold more robust repression of translation compared to a mixture of DDX3X (6 μM) and MBP (2 μM). Moreover, a mixture of DDX3X (2 μM) and DDX3Y (6 μM) less efficiently repressed translation relative to DDX3Y (8 μM) alone. Furthermore, the *in vitro* LLPS assays were performed with different ratios of DDX3X and DDX3Y in the presence of

RNA. The addition of DDX3Y to DDX3X stimulated droplet formation, and condensation was positively correlated with the relative amount of DDX3Y (Figure 6C).

DDX3Y more strongly promotes FUS aggregation than DDX3X

Dysregulation of SGs can promote FUS aggregation, leading to cell death (Bentmann et al., 2012; Guo et al., 2018; Kamelgarn et al., 2016; Silva et al., 2019). Thus, we studied how DDX3X and DDX3Y influence *in vitro* FUS fibrillization. When we added 1 μM wild-type FUS to either DDX3X or DDX3Y, we saw that the aggregation of FUS, detected by light scattering at 395 nm, was enhanced by both helicases but was more extensively aggravated in the presence of DDX3Y (Figure S6E). To quantify the effect of DDX3X and DDX3Y on FUS aggregation over time, we measured the area under the curve (AUC) for each scattering time course. Both DDX3X and DDX3Y enhance FUS aggregation but that DDX3Y had a stronger enhancement, even at high concentrations of either protein (Figures 6D and S6E). We also studied the colocalization of FUS and DDX3X or DDX3Y in HeLa cells upon arsenite treatment. We constructed a DOX-inducible stable cell line that expressed FUS. As shown in Figure 6E – 6F, while wild-type FUS was mainly located in the nucleus with transfection of empty vector, a portion of FUS formed puncta which colocalize with DDX3X-positive granules and DDX3Y-positive granules in the cytoplasm with transfection of DDX3X and DDX3Y expression plasmids. Furthermore, DDX3Y-FUS puncta were significantly larger than DDX3X-FUS puncta (Figure 6G). As XY individuals are at a higher risk for developing ALS (Manjaly et al., 2010), these data not only suggest that DDX3X and DDX3Y affect FUS aggregation but also suggest that the enhanced propensity to promote LLPS by DDX3Y might lead to a XY-specific increase of FUS aggregation.

DDX3Y more strongly accelerates TDP-43 aggregation than DDX3X

Finally, we tested whether DDX3X or DDX3Y might also stimulate the aggregation of TDP-43, another prominent RNA-binding protein connected to ALS and FTD (Portz et al., 2021; Tan et al., 2017). We found that DDX3X or DDX3Y did not enhance the total amount of TDP-43 aggregation (Figure S6F and S6G). However, both helicases accelerated TDP-43 aggregation (Figure S6F and S6H). The halftime $t_{1/2}$ (i.e. the time at which 50% TDP-43 aggregation had occurred) was reduced from ~6.9 hrs in the absence of helicase to ~5.7 hrs in the presence of DDX3X and ~ 4.4 hrs in the presence of DDX3Y (Figure S6F and S6H). These findings suggest that DDX3Y can accelerate TDP-43 aggregation more potently than DDX3X.

DISCUSSION

Herein, we report the first comparative study of the sexually dimorphic RNA helicases DDX3X and DDX3Y in the regulation of translation via distinct phase separation behaviors (Figure 6H). Importantly, we reveal the molecular mechanism underpinning the higher propensity of DDX3Y to phase separate and its lower propensity to disassemble once condensed. Firstly, we find that the condensation propensity differences of DDX3X and DDX3Y are most likely due to the sequence composition of both IDR1s. Overall, the percentages of both negatively and positively charged amino acids in Y^{IDR1} (17.3% and 16.1% respectively) are higher than in X^{IDR1} (16.7% and 14.9% respectively), whereas

the percentage of charged amino acids is similar between the other domains of DDX3X and DDX3Y (Figure S6I). This finding suggests that Y^{IDR1} can form more charge-charge interactions to support phase separation. In addition to these electrostatic interactions, cation-π and π-π (Vernon et al., 2018) interactions are known to facilitate LLPS (Qamar et al., 2018). As such, Tyr to Phe and Arg to Lys mutations in IDRs dramatically impair phase separation (Schuster et al., 2020). In line with this, Phe84 and Lys118 in X^{IDR1} correspond to Tyr83 and Arg116 in Y^{IDR1}, suggesting that Y^{IDR1} is capable of more cation-π and π-π interactions than X^{IDR1}, which might result in the stronger phase separation of DDX3Y found in these studies (Figure S1A). Indeed, Lys118 in DDX3X is a known site of post-translational acetylation (Saito et al., 2019). Acetylation at this site decreases the phase separation of DDX3X *in vitro* and inside of cells through the disruption of cation-π interactions. Given that the analogous position in DDX3Y is an arginine (Arg116), which is often thought of as a "non-acetyl" mimetic, this position is likely a key source of difference between DDX3X and DDX3Y and merits future study.

Second, our data suggest that the distinct dynamics of DDX3X- and DDX3Y-positive SGs may also be related to differences in their ATPase-driven SG remodeling activity (Jain et al., 2016; Tauber et al., 2020) (Figure 4). Furthermore, the differences in dynamics of DDX3X and DDX3Y condensates may also explain why DDX3Y more strongly repressed translation than DDX3X. DDX3X-positive SGs and DDX3Y-positive SGs sequester distinct mRNAs in addition to a shared pool of transcripts, suggesting that the differences in ATPase activity and translational repression may have functional consequences, especially under stress (Figure 5G – 5K). The results shared here suggest that DDX3X and DDX3Y might influence the translation of the overlapping mRNA targets to different degrees in addition to exerting differential regulation of distinct RNA components. They might also differentially sequester other translational components.

One important question that remains to be answered is the degree to which DDX3X and DDX3Y overlap functionally. Studies by others have suggested that DDX3X and DDX3Y are redundant in protein synthesis under unstressed conditions (Venkataramanan et al., 2021). Our data suggest that their divergent roles may not be apparent until they are driven to phase separate during the stress response.

Stress leads to various human disorders, many of which display sex-biased features. For instance, ALS is ~20% more common in males than females (Manjaly et al., 2010). We showed that DDX3Y more strongly promotes FUS self-assembly *in vitro* and formed larger FUS granules in cells (Figure 6D – 6G), possibly through its stronger phase separation propensity compared to DDX3X. Furthermore, DDX3Y more strongly accelerated TDP-43 aggregation than DDX3X (Figure S6F – S6H). Other known SG resident proteins such as TIA-1, hnRNPA1, and hnRNPA2 have been previously indicated in ALS (Fernandes et al., 2020; Gilks et al., 2004; Harrison and Shorter, 2017; Khalfallah et al., 2018; Molliex et al., 2015). Future investigation on the scope and extent of DDX3X's and DDX3Y's impact on these proteins in sex specificity in neurodegenerative diseases will be exciting.

Limitations of the Study

HeLa cells may not be perfectly suited to the task of uncovering the biological targets in DDX3Y-specific SGs, because they lack a Y chromosome and thus may also lack some of the specific transcripts that may be targeted by DDX3Y. However, we feel that reconstituting HeLa cells (with endogenous DDX3X depleted) with ectopically expressed DDX3X or DDX3Y provided a clean system to reveal the different RNA sequestration impacts of DDX3X and DDX3Y due to their intrinsic differences in phase separation. Thus, we believe our findings are an excellent proof of principle. Additionally, while our recombinant proteins were purified to apparent homogeneity and are not expected to have unequal carryover of RNA, there could be some effect of potential impurities on the magnitude of the differences we measure. However, we believe that the difference itself is a true observation about these proteins. The apparent unwinding activity observed in the smFRET assays is not an indication of complete unwinding by DDX3X/DDX3Y and this assay is not a conventional assay to study helicase activity. Both the donor and acceptor fluorophores being present in all molecules compiled in the smFRET analysis indicates only partial unwinding of the RNA substrate. We believe our smFRET assay is mainly reflecting the ATPase and dynamic activity of the proteins with RNA and give insight into the differences between DDX3X and DDX3Y in these features. Our experiments should serve as a crucial first step towards understanding the role of sexually dimorphic proteins in disease.

STAR METHODS

RESOURCE AVAILABILITY

Lead contact—Further information and requests for resources and reagents should be directed to and will be fulfilled by the Lead Contact, Kathy Fange Liu (liufg@pennmedicine.upenn.edu).

Materials availability—All materials generated in this study are available on request to Lead Contact.

Data and code availability

- RNA-seq data have been deposited at GEO and are publicly available as of the date of publication. Accession numbers are listed in the key resources table. Original western blot images have been deposited at Mendeley and are publicly available as of the date of publication. The DOI is listed in the key resources table. Microscopy data reposted in this paper will be shared by the lead contact upon request.

- This paper does not report original code.

- Any additional information required to reanalyze the data reported in this paper is available from the lead contact upon request.

EXPERIMENTAL MODEL AND SUBJECT DETAILS

Cell culture, transfection and *Escherichia coli* strains—HeLa, HEK293T, and N2a cells were cultured in DMEM + GlutaMAX (GIBCO) with 10% FBS (GIBCO) and 1% Pen/Strep (Corning) in a humidified incubator with 5% CO_2 at 37°C.

For bacterial cell culture, TOP10 and BL21(DE3)-RIL chemically competent bacterial strains grew in lysogeny broth containing the corresponding antibiotics at 200 rpm, 37°C.

The negative control siRNA from Ambion (AM4611) was used as a control siRNA in the knockdown experiments. DDX3X siRNA was purchased from Ambion (Assay ID 145803). Lipofectamine 2000 (Invitrogen) and Lipofectamine RNAiMax (Invitrogen) from Invitrogen were used for plasmids and siRNA transfection, respectively. It took 48 hrs for siRNA knockdown and 24 hrs for plasmid expression.

METHOD DETAILS

Constructs—For recombinant MBP-DDX3X and MBP-DDX3Y protein expression: DNA fragments encoding human DDX3X were PCR-amplified from the HeLa cDNA library, and the human DDX3Y coding sequence was PCR-amplified from pCMV6-DDX3Y (Origene RC226072). These DNA fragments were then inserted into the pMAL-c2x vector (Walker et al., 2010) (Addgene Plasmid #75286) using restriction enzymes BamHI and SalI. A TEV enzyme digestion sequence (protein sequence ENLYFQG; DNA sequence GAAAACCTGTACTTCCAGGGA) was added to the forward primers, and a His-tag sequence (protein sequence HHHHHH; DNA sequence CATCATCACCATCACCAC) was added to the reverse primers. For *in vitro* LLPS experiments, the pETMCN_His-TEV_V5-DDX3Y-mCherry construct was made by swapping the DDX3Y with the DDX3X in the pETMCN_His-TEV_V5-DDX3X-mCherry (Hondele et al., 2019) using NdeI and BamHI restriction enzymes. For expression of DDX3X and DDX3Y in mammalian cells, DNA fragments encoding the full-length DDX3X and full-length DDX3Y were inserted into the pPB vector with FLAG (DYKDDDDK) and HA (YPYDVPDYA) tags before the N-terminus of the proteins using MfeI and SalI (XhoI was used for digesting the pPB vector) restriction enzymes. The plasmids expressing FLAG or HA single-tagged DDX3X and DDX3Y were made by inserting the DNA fragments encoding full-length DDX3X or full-length DDX3Y into the modified pcDNA3 vector with FLAG or HA tag in frame at the N-terminus.

For the truncation variants of DDX3X and DDX3Y, the following truncations were put into the pPB vector (domain prediction based on PONDR (Xue et al., 2010)): IDR1 of DDX3X (amino acids 1–168); IDR1 of DDX3Y (amino acids 1 – 164); IDR2 of DDX3X (amino acids 580 – 662); IDR2 of DDX3Y (amino acids 579 – 660); helicase domain of DDX3X (amino acids 169 – 579); helicase domain of DDX3Y (amino acids 165 – 578);   IDR1 truncation variant of DDX3X (amino acid 169 – 662);   IDR1 truncation variant of DDX3Y (amino acids 165 – 660);   IDR2 truncation variant of DDX3X (amino acids 1 – 579);   IDR2 truncation variant of DDX3Y (amino acids 1 – 578);   Helicase truncation variant of DDX3X (amino acids   169 – 579);   Helicase truncation variant of DDX3Y (amino acids   165 – 578). For domain-swap variants of DDX3X and DDX3Y, the following constructs were inserted into the pPB vector:

DDX3X^{IDR1}-DDX3Y^{Helicae}-DDX3Y^{IDR2}; DDX3YIDR1-DDX3XHelicae-DDX3XIDR2; DDX3XIDR1-DDX3Xhelicae-DDX3YIDR2; DDX3YIDR1-DDX3Yhelicae-DDX3XIDR2; DDX3XIDR1-DDX3Yhelicae-DDX3XIDR2; DDX3YIDR1-DDX3Xhelicae-DDX3YIDR2. DDX3X-EGFP, DDX3X-mCherry, DDX3Y-EGFP, and DDX3Y-mCherry with a linker sequence (amino acids GlyGlySerGly) inserted between DDX3X/DDX3Y and EGFP/mCherry were inserted into the pPB vector using MfeI and SalI restriction enzymes. Those domain-swap variants were cloned into the pETMCN_His-TEV_V5-mCherry vector to express mCherry-tagged proteins in *E.coli* as well.

For APEX2-seq experiments, the DNA fragment encoding APEX2 was PCR amplified from pcDNA5/FRT/TO APEX2-GFP (Addgene, 129640) and fused to DDX3X and DDX3Y using fusion PCR. APEX2-DDX3X and APEX2-DDX3Y were inserted into the pPB vector using MfeI and Sal I restriction enzymes, and APEX2-EGFP was inserted into the pPB vector using MfeI and XhoI restriction enzymes. To validate the biotin labeling efficiency of APEX2, the plasmid pPB mito-APEX2 was constructed. The DNA fragment encoding a mitochondria matrix localization sequence (amino acids MLATRVFSLVGKRAISTSVCVRAH) derived from *COX4* was added to the APEX2 forward primer for the PCR reaction. The PCR product was subsequently inserted into the pcDNA3 vector by using BamHI and XhoI restriction enzymes.

All the sequences of the primers used for these clones are summarized in Table S3, and each plasmid was validated by Sanger sequencing.

Protein purification—The pMAL-c2X-DDX3X, pMAL-c2X-DDX3Y plasmids were transformed into *Escherichia coli* strain BL21-RIL to express the MBP-tagged recombinant proteins. The pETMCN_His-TEV_V5-DDX3X-mCherry (Hondele et al., 2019), pETMCN_His-TEV_V5-DDX3Y-mCherry and other domain-swap variants in the pETMCN_His-TEV_V5-mCherry vectors were transformed into *E. coli* strain BL21-RIL to express the mCherry-tagged recombinant proteins. The bacteria were cultured in lysogeny broth at 37°C till $OD_{600\ nm}$ = 0.8 before administration of 1 mM IPTG at 16°C for 16 hrs. The pellets from 2 L bacterial culture were resuspended with 80 mL binding buffer (25 mM Tris-HCl, pH 7.5, 500 mM NaCl) and sonicated. After centrifuging at 12,000 rpm for 30 min to remove the cell debris, the supernatant was loaded to a Ni-NTA column. Next, 10 column volumes of the binding buffer supplemented with 50 mM imidazole was used as buffer A to wash away the non-specific binding proteins. Another 10 column volumes of a high salt buffer (25 mM Tris-HCl, pH 7.5, and 2 M NaCl) was used to decrease the amount of bound RNAs from DDX3X or DDX3Y. Finally, four column volumes of the binding buffer supplemented with 500 mM imidazole was used to elute the bound proteins. The DDX3X-mCherry and DDX3Y-mCherry recombinant proteins were dialyzed into the storage buffer (25 mM Tris-HCl, pH 7.5, 500 mM NaCl, 10% glycerol, and 2 mM DTT) and the His-tag was cleaved using TEV enzyme simultaneously with the dialysis. Then, the proteins were concentrated using Amicon Ultra-15 (Millipore) tubes before loading to a Superdex 200 column, with buffer (25 mM Tris-HCl, pH 7.5, and 500 mM NaCl) for mCherry tagged proteins and buffer (25 mM Tris-HCl, pH 7.5, 200 mM NaCl) for MBP tagged proteins. MBP-tagged proteins were purified at 4°C, while mCherry-tagged proteins were purified at room temperature. The purity of the proteins was analyzed by SDS-PAGE.

Purified proteins were aliquoted, snap-frozen in liquid nitrogen and stored at −80°C. Once thawed, aliquots were never refrozen.

GST-TEV-FUS^{WT} was purified as described (Sun et al., 2011). Briefly, *E. coli* cells were lysed by sonication on ice in PBS with protease inhibitors (cOmplete, EDTA-free, Roche Applied Science). The protein was purified over Glutathione Sepharose 4 Fast Flow (GE Healthcare) and eluted from the beads using 50 mM Tris-HCl pH 8, 20 mM trehalose, and 20 mM glutathione. Purified protein was snap-frozen in liquid nitrogen and stored at −80°C.

pJ4M/TDP-43 was a gift from Nicolas Fawzi (Addgene plasmid # 104480). TDP-43 was purified as previously described (Hallegger et al., 2021). Briefly, the plasmid was transformed into BL21(DE3) RIL *E. coli.* Cells were harvested by centrifugation and lysed by lysozyme (1 mg/mL) and sonication in wash buffer (20 mM Tris-HCl pH 8.0, 1 M NaCl, 10 mM imidazole, 10% glycerol, 1 mM DTT, 5 μM Pepstatin A, 100 μM PMSF, and cOmplete, EDTA-free, Roche Applied Science protease inhibitors). The protein was purified over Ni-NTA agarose beads (QIAGEN) and eluted from the beads using elution buffer (wash buffer except with 300 mM imidazole rather than 10 mM imidazole). The protein was further purified over amylose resin (NEB) and eluted with 20 mM Tris-HCl pH 8.0, 1 M NaCl, 10 mM imidazole, 10% glycerol, 1 mM DTT, 5 μM Pepstatin A, 100 μM PMSF, and 10 mM maltose. The protein was concentrated, snap-frozen in liquid nitrogen, and stored at −80°C.

Differential scanning fluorimetry assay—Purified MBP-DDX3X and MBP-DDX3Y proteins were diluted to 0.25 mg/mL. 19 μL of each protein was transferred to a well of a 384-well plate, and 1 μL of 5-fold SYPRO Orange (Thermo Fisher) was added to each well. The plate was sealed and spun at 3,600 *g* for 2 min. The fluorescent signal at 570 nm was collected using a RT-qPCR machine with the temperature ramping from 20 to 95°C. The data were analyzed using DSF World (Wu et al., 2020).

***In vitro* LLPS assay—**The *in vitro* LLPS was set up at room temperature with total volume of 20 μL in PCR tube. Proteins were diluted to 100 μM (DDX3X-mCherry and DDX3Y-mCherry) or 75 μM (DDX3X-mCherry, DDX3Y-mCherry and all the domain-swap mutants) using the storage buffer. 10 μL buffer (25 mM Tris-HCl, pH 7.5, 500 mM NaCl) and 2 μL diluted protein were transferred to the PCR tube. Then, 8 μL water was added to the tube to observe the LLPS of protein alone; 2 μL polyU-RNA (2 mg/mL, dissolved in water) and 6 μL water were added to the tube to observe the LLPS of protein with RNA; 2 μL polyU-RNA (2 mg/mL, dissolved in water), 2 μL ATP buffer (40 mM ATP and 50 mM MgCl$_2$) or UTP buffer (40 mM UTP and 50 mM MgCl$_2$) and 4 μL water were added to the tube to observe the LLPS of protein with RNA and ATP or UTP. To observe the LLPS of different combinations of DDX3X-mCherry and DDX3Y-mCherry, the proteins were diluted to the proper concentrations. Then 10 μL buffer, 2 μL diluted protein and 8 μL water were transferred to a PCR tube. The mixtures were mixed by pipetting and transferred to 384-well glass-bottomed plate. After incubating at room temperature for 1 hr, the plate was spun at 100 *g* for 1 min. Then the images were taken using a Zeiss LSM 880 confocal microscope under a 63 × oil lens.

Immunofluorescence cell staining—Cells were passaged to a 6-well plate with a coverslip in each well and cultured overnight. The cells were washed once in PBS and then fixed using 4% paraformaldehyde in PBST (PBS with 0.05% Tween-20) at room temperature for 15 min. Then, the cells were washed twice by PBST and permeabilized by 0.5% Triton at room temperature for 20 min. After being washed once by PBST, the cells were blocked with 1% BSA in PBST at room temperature for 30 min. Then, the blocking solution was replaced with 1 mL blocking solution supplemented with desired primary antibodies (at 1:1000 dilution) and incubated at room temperature for 1 hr or 4 °C overnight. After 4 washes with PBST, the corresponding Alexa Fluor-conjugated secondary antibodies were applied (1:1,000 diluted in the blocking solution) and incubated at room temperature for 1 hr. After being washed three times by PBST, the cells were incubated with 0.5 μg/mL DAPI for 1 min. After 4 times PBST washes, an antifade reagent (Invitrogen) was used to mount the slides. The images were taken using a Leica TCS SP8 confocal microscope. The "analyze particles tool" in Fiji (Schindelin et al., 2012) was utilized to quantify the sizes of the stress granules in mammalian cells in about 50 different cells per condition. The sizes of the stress granule in cells were analyzed by two researchers independently.

Fluorescence recovery after photobleaching—The FRAP assays were conducted using the bleaching module of the Zeiss LSM 880 confocal microscope for DDX3X and DDX3Y droplets individually. The 488 nm laser was used to bleach the EGFP signal, and the 561 nm laser was used to bleach the mCherry signal. Bleaching was focused on a circular region of interest (ROI) using 100% laser power, and time-lapse images were collected afterward. A same-sized circular area away from the bleaching point was selected as an unbleached control. The fluorescence intensity was directly measured in the Zen software. The values were reported as relative to pre-bleaching time points. GraphPad Prism was used to plot the data. The halftime for each replicate was calculated using the following formula: $y=a \cdot (1-exp(-b \cdot x)) + c$, in which a is the slow recovery fraction, c is the rapid diffusion fraction, and b is the recovery rate. The halftime is $\ln 2 / b$, and a mobile fraction is $a + c$. The two-tail t-test was used to calculate the p-values. For FRAP of the live cells, cells expressing DDX3X-EGFP or DDX3Y-EGFP were cultured in 35 mm poly-D-lysine coated glass-bottomed dishes (Mattek). Before taking the images, cells were treated with 500 μM sodium arsenite for 1 hr in the FluoroBrite DMEM medium with 10% FBS. A 20 × lens was used at zoom scale 6. For FRAP of *in vitro* LLPS, a 63 × oil lens was used.

Formation of stress granules in cells—Cells were seeded in a 6-well plate and cultured overnight. The following stressors: 500 μM sodium arsenite (1 hr), 1 M sorbitol (1 hr), 50 μM thapsigargin (1 hr), 40 μg/mL puromycin (3 hrs), and 10 μM MG132 (3 hrs) were added to the cell culture media (DMEM + 10% FBS) each in a separate well. For the stress condition of 60 μM CCCP, CCCP was added to glucose-free DMEM with 10% FBS. After the treatment, cells were fixed and subjected to the immunofluorescence imaging procedure detailed above.

Sequence alignment—The amino acid sequences of DDX3X and DDX3Y were downloaded from CCDS Database and aligned using Clustal Omega. The alignment results were redrawn using ESPript 3.0 (Robert and Gouet, 2014). The sequences were used to

predict the natural disordered regions by PONDR (Xue et al., 2010), prion-like amino acid regions by PLAAC (Lancaster et al., 2014) and LLPS propensity by catGRANULE (Mitchell et al., 2013).

Turbidity assay—DDX3X-mCherry and DDX3Y-mCherry proteins were diluted to 10, 20, 30, 50, 75, 100, 125 and 150 μM using the storage buffer. 15 μL buffer (25 mM Tris-HCl, pH 7.5, 200 mM NaCl), 3 μL diluted protein were transferred to the PCR tube, 3 μL polyU-RNA (2 mg/mL, dissolved in water), and 9 μL water were mixed in a PCR tube. After incubating for 20 min at room temperature, the mixtures were transferred to a 384-well black plate with a clear flat bottom. The turbidity was measured by using a Tecan plate reader at $OD_{600\ nm}$. Then, the solution was transferred to a clean Eppendorf tube, and spun at 16,000 g for 2 min. The supernatant was used to measure protein concentration using Bradford method.

Construction of DOX-inducible cell lines—5 μg of the lentiviral vectors expressing mClover3-FUS, 2.5 μg VSVG plasmid, and 3.75 μg pPAX2 plasmid were co-transfected to 100% confluent HEK 293T cells in 6-well plate with 40 μL polyethylenimine. The medium was changed after 6 to 8 hrs. 500 μL medium containing the virus was collected twice a day and 500 μL fresh medium was replenished at each time. The virus was collected in a total three-day period, and then spun down at 3000 rpm for 5 min at room temperature. The HeLa cells were infected with lentivirus with 8 μg/mL polybrene. After induction with 100 ng/mL of doxycycline (DOX) for two days, the cells were subjected to cell sorting. Western blots were performed to validate the expression of mClover3-FUS by using anti-GFP antibody.

Colocalization of DDX3X/Y with FUS in cells—The DOX-inducible HeLa cells expressing mClover3-FUS were seeded in a 6-well plate with 100 ng/mL of DOX and a coverslip in the well. 1 μg of empty vector, DDX3X-pPB, or DDX3Y-pPB were transfected to those cells respectively using lipofectamine 2000. 24 hrs later, sodium arsenite was used to each well at a final concentration of 500 μM for 1 hr. The cells were then subjected to the immunofluorescence cell stain protocol as discussed above.

Cycloheximide chase assay—The cycloheximide (CHX) chase assay was performed to explore the half-life of DDX3X and DDX3Y proteins in cells. HeLa cells were seeded in 6-well plate and transfected with 1 μg of DDX3X-pPB and DDX3Y-pPB respectively. 24 hrs later, CHX was added to the cells at a final concentration of 100 μg/mL and incubated for different time intervals. Then, the cells were collected and lysed with RIPA buffer (25 mM Tris-HCl, pH 7.4, 150 mM NaCl, 2 mM EDTA, and 1% NP-40). The protein concentrations were measured using a Bradford assay and the same amount of cell lysate was used in Western blot analyses. The intensity for each band was quantified using Fiji. The intensity for each DDX3X and DDX3Y band was normalized to the corresponding GAPDH intensity firstly, and then for each replicate at different time points were normalized to time 0 hr. The data were plotted in Prism and an exponential decay formula was used to determine the half-life of DDX3X and DDX3Y. The degradation rate K_{decay} was estimated by $\ln(A_t/A_0) = -K_{decay}\ t$ where A_t and A_0 stand for the quantity at time t and time 0. Thus, the half-life ($t_{1/2}$), when 50% of the protein is decayed is described by $t_{1/2} = \ln2\ /\ K_{decay}$.

Puromycin incorporation assay—HeLa cells were seeded in a 6-well plate with a coverslip in it, and then transfected with 1 μg of pPB-DDX3X and pPB-DDX3Y respectively. After 24 hrs, a final concentration of 500 μM sodium arsenite was added to the DMEM and incubated for 5 min to trigger stress granule formation. Then, the medium was replaced by fresh DMEM medium with puromycin (1 μg/mL). After incubating for 30 min in a humidified incubator with 5% CO_2 at 37°C, the cells were then washed with 1 × PBS and subjected to the immunofluorescence cell staining protocol as described above using anti-puromycin and anti-FLAG antibodies.

Malachite green ATPase assay—ATPase measurements were taken using the Malachite Green Phosphate Assay Kit according to the manufacturer's instructions. Briefly, 1.0 μM MPB-DDX3X or MBP-DDX3Y was incubated with 100 ng/μL total RNA extracted from HeLa cells for 15 min in the reaction buffer (25 mM Tris-HCl, pH 8, 200 mM NaCl, 1 mM DTT, and 2 mM $MgCl_2$) before the addition of 2 mM ATP. The reaction was incubated at room temperature for 30 min. Then the reaction was quenched by the addition of malachite green mixture and left for an additional 30 min to develop the color. The samples were then loaded into a clear-bottom 384-well plate and absorbance at $OD_{600\ nm}$ was measured. Values were converted from absorbance units to μM free phosphate using a standard curve generated with the kit's phosphate standard. Background values (free phosphates detected from reactions lacking RNA) were subtracted from the value from reactions with RNA. Data were plotted in Prism. Significance was calculated using Student's two-tailed t test.

Continuous ATPase assay—ATPase measurements were taken using the EnzChek Phosphate Assay Kit (ThermoFisher) as previously described (Song and Ji, 2019). Briefly, MBP-DDX3X or MBP-DDX3Y was titrated at the indicated concentrations into 500 μL reactions containing 40 mM Tris-HCl pH 7.5, 50 mM NaCl, 0.5 mM $MgCl_2$, 2 mM DTT, 0.5 units Super RNaseIN, 0.01% NP-40 substitute and 100 nM annealed duplex RNA (sequence in Table S3). After 10 min of incubation at room temperature, the reaction was started by adding 2 mM magnesium ATP. The reaction progress was monitored over five min at 30 sec intervals as absorbance at 360 nm. Absorbance values were the converted to μM/min using a standard curve and initial rates were plotted and fit to Hill kinetics using Prism.

smFRET—PEG-passivated slides were prepared according to previously published protocols with minor modifications (Jamiolkowski et al., 2017). Briefly, glass coverslips and slides were sonicated at 40°C twice with acetone for 15 min followed by sonication with methanol (25 min), 1 M KOH (40 min), and ethanol (15 min). Plasma cleaning was then used to remove any remaining contaminants from the surfaces. Plasma cleaned slides and coverslips were then incubated in a solution composed of 1.4 mL of 3-aminopropyltriethoxysilane (APTES), 2.3 mL of glacial acetic acid, and 46 mL of methanol overnight at room temperature. Silicated slides and coverslips were then incubated with polyethylene glycol (PEG, Laysan Bio, Inc., containing 20% (w/w) mPEG succinimidyl valerate, MW 2000 and 1% biotin-PEG-SC, MW 2000) in 0.1 M sodium bicarbonate (pH 8.3) for four hrs followed by an additional incubation overnight in a humidifying chamber. Slides and coverslips were then washed with MilliQ water and used to construct flow

chambers for single molecule experiments with double-sided sticky tape. Double stranded RNA with a 5' overhang was obtained as follows: 5'-biotin/ACCGCUGCCGUCGCUCCG/ AlexF647N/–3'; and 5'-/Cy3/ UUUUUUUUUUUUUUUUUUUUUUUUUUUUUUUUUUUUUUUUUUUUUUUUUUC GGAGCGACGGCAGCGGU-3' were ordered from IDT; the two strands were annealed by heating the sample at 65°C for 5 min, then slowly cooling the sample to room temperature over 3 hrs. 2 mM protocatechuic acid (PCA), 0.05 uM protocatechuate-3,4,dioxygenase, 2.45 mM 6-hydroxy-2,5,7,8- tetramethylchromane-2-carboxylic (Trolox), 1 mM cyclooctatetraene (COT), and 1 mM 4-nitrobenzyl alcohol (NBA) were added to the imaging buffer (125 mM NaCl and 50 mM Tris-HCl pH 7.5). 70 pM biotinylated, fluorescent dsRNA was added to the flow cell and incubated for 6 min. Unbound RNA was washed out and recording either commenced or DDX3X or DDX3Y were first added as indicated in the text. The TIRF microscope, optics and camera were used to record smFRET as in previous report (Jamiolkowski et al., 2017). All FRET measurements were carried out at room temperature (~23°C) using a frame interval of 100 ms with alternating 532 nm/640 nm laser excitation (ALEX; effective frame interval 200 ms). Data analyses were carried out using custom scripts written in either Python or Java. Background-corrected fluorescence intensities and FRET distributions were corrected for differential quantum yield, differential detector sensitivity, direct excitation of the A647 by the 532 nm laser and leakage of Cy3 fluorescence into the acceptor detector channel as in previous report (Hellenkamp et al., 2018; Jamiolkowski et al., 2017). Only recordings exhibiting a single step photobleaching event in the direct acceptor excitation (ALEX) channel were further analyzed and included in FRET distributions.

RNA isolation—A Direct-zol RNA MicroPrep kit (Zymo Research) was used to isolate total RNA following the manufacturer's instructions. DNA digestion was performed on the column at room temperature for 15 min to remove the DNA contamination of the extracted RNA. For a larger scale of RNA purification, total RNA was purified by TRIzol reagent (Invitrogen), following the manufacturer's instruction.

RT-qPCR—RT-qPCR was performed using a Luna Universal One-Step RT-qPCR kit (NEB) to assess the relative abundance of RNA in each sample. All samples used for RT-qPCR were treated with DNase I to remove possible DNA contamination. The primers used for RT-qPCR are listed in Table S3.

Cellular APEX labeling—To enable APEX labeling in mammalian cells, we followed a previously established protocol (Fazal et al., 2019). Briefly, the cells were treated with or without 500 μM sodium arsenite in DMEM media for 30 min. Then, the DMEM media with 500 μM sodium arsenite was replaced with DMEM media supplemented with 500 μM sodium arsenite and 500 mM biotin-phenol for another 30 min. Next, H_2O_2 (Sigma-Aldrich) was added to each cell culture dish at 1 mM final concentration for exactly 1 min with gentle agitation. To stop the labeling, the culture media was removed, and the quenching solution (10 mM sodium ascorbate, 10 mM sodium azide, and 5 mM Trolox in PBS) was immediately used to wash the cells three times. Finally, 1 mL quenching solution was applied to cover the cells. Cells were then collected with a cell scraper. The unlabeled

control samples were prepared in parallel under the same procedure as aforementioned, without the addition of the H_2O_2.

Validation of APEX labeling—To validate APEX labeling in cells, after the cellular labeling reaction, the cells were lysed using RIPA buffer (25 mM Tris-HCl, pH 7.4, 150 mM NaCl, 2 mM EDTA, and 1% NP-40) supplemented with 10 mM sodium ascorbate, 10 mM sodium azide, 5 mM Trolox, and proteinase inhibitor on ice for 15 min. After centrifugation, the supernatant of the cell lysate was loaded on an SDS-PAGE gel and transferred to a PVDF membrane (Millipore) by a semi-dry transfer instrument. The membrane was blocked with 5% BSA in PBST at 4 °C overnight. 1:20,000 diluted streptavidin-HRP antibody (cell signaling) in 5% BSA was used at room temperature for 1 hr to detect the biotinylated proteins. After washing three times with PBST, the membrane was visualized by ECL Western Blotting Detection Kit (Thermo Fisher). The endogenous biotinylated proteins were also visible at 130, 75, and 72 kDa in both the labeled and unlabeled cells (as expected).

Purification and sequencing biotinylated RNA—After the cellular APEX-labeling, total RNA was extracted using TRIzol following the manufacturer's instruction. To enrich biotinylated RNAs, Pierce streptavidin magnetic beads (Thermo Fisher) were used (20 μL beads per 50 μg RNA). The beads were washed 3 times with 500 μL B&W buffer (5 mM Tris-HCl, pH 7.5, 0.5 mM EDTA, 1 M NaCl, and 0.1% TWEEN 20), followed by 2 times with 500 μL solution A (0.1 M NaOH and 50 mM NaCl), and once with 500 μL solution B (100 mM NaCl). The beads were then suspended in 125 μL solution B. 50 μg RNA diluted in 125 μL water was mixed with the beads and incubated at 4 °C for 2 hrs with rotation. Then, the beads were placed on a magnetic stand to remove the solution and washed 3 times with 500 μL B&W buffer. Finally, the beads were resuspended in 54 μL water. To release the biotinylated RNA, 33 μL proteinase buffer (3 × PBS, 6% N-Lauryl sarcosine sodium solution (Sigma-Aldrich), 30 μM EDTA, and 15 μM DTT) was added to the beads with 10 μL proteinase K (Thermo Fisher) and 5 μL RNase inhibitor. The beads were then incubated at 42 °C for 1 hr and 55°C for 1 hr on a shaker at 600 rpm. The RNA was then purified using a RNA Clean and Concentrator 5 kit (Zymo Research) following the manufacturer's instruction. The resulting RNA was then used for RNA-seq library construction using a TruSeq Stranded mRNA Kit (Illumina). The concentrations for all the libraries were determined by KAPA Library Quantification Kit (KAPA Biosystems) following the manufacturer's protocol and subjected to Next-generation high-throughput sequencing using an Illumina NextSeq 550 with a single-end 75-bp read length.

Validation of the APEX labeling of RNA—To test the specificity of APEX2 labeling, APEX2 was fused with a mitochondrial localization signal (MLATRVFSLVGKRAISTSVCVRAH, derived from *COX4*) at its N terminus. The localization of the fused protein was validated by immunofluorescence. Total RNA was first extracted from the labeled and unlabeled cells, which was then followed by enrichment of biotinylated RNA using the streptavidin magnetic beads as described above. To test for the RNA enrichment, primers against mitochondria-translated transcripts *ND1* and *ND2*, and cytoplasm translated transcripts *GAPDH* and *TRMT10A* were designed and listed in

Table S3. RT-qPCR was performed in the labeled and unlabeled controls. The ratios of RNA recovered in the labeled samples relative to unlabeled controls were calculated.

High throughput data analysis—The high throughput sequencing reads were adaptor and quality trimmed using Trimmomatic (Bolger et al., 2014) with the following command: trimmomatc SE -phred33 ILLUMINACLIP:TruSeq3-SE.fa:2:30:10 LEADING:3 TRAILING:3 SLIDINGWINDOW:4:15 MINLEN:30. Then, the reads were aligned to the GRCh38 human genome reference using HISAT2(Kim et al., 2015). The default parameters were used. Aligned reads were quantified using featureCounts (Liao et al., 2014). Read counts were further analyzed using DESeq2 (Love et al., 2014). Gene ontology (GO) analysis was carried out with the Metascape (Zhou et al., 2019).

In Vitro* translation—In vitro* translation assays were performed using the Flexi Rabbit Reticulocyte Lysate System (Promega). Each reaction (25 μL) contains 10 μL rabbit reticulocyte lysate, 0.25 μL amino acid mixture minus leucine (1 mM), 0.25 μL of amino acid mixture minus methionine (1 mM), 1 μL Mg(OAc)2, 0.25 μL luciferase mRNA (1 mg/mL), 0.5 μL RNase inhibitor, 0.25 μL DTT (1 M), and 12.5 μL of different concentrations of DDX3X-mCherry, DDX3Y-mCherry, or buffer (25 mM HEPES-KOH, pH 7.4, 150 mM KCl, and 2 mM DTT). Assembled reactions were incubated at 30°C for 90 mins. A standard reaction containing 75 μL of the luciferase substrate mixed with 5 μL of the unpurified translation mixture in a white 96-well plate. The luminescence was measured using a luminometer (Promega). To observe any LLPS in the lysate, the lysate from the translation assays was transferred to 384-well glass-bottomed plate. Then, the plate was spun at 100 g for 1 min. The images were taken using a Zeiss LSM 880 confocal microscope under a 63 × oil lens.

FUS aggregation assay—First, 0, 0.25, or 0.5 μM MBP-TEV-DDX3X or MBP-TEV-DDX3Y was incubated with 1 μg TEV protease for 30 min at room temperature. Then, 1 μM GST-TEV-FUS[WT] (or an equal volume of elution buffer) was added to the reaction and turbidity was used to assess aggregation by measuring absorbance at 395 nm in a Tecan plate reader. Readings from DDX3X or DDX3Y alone were subtracted from the appropriate FUS conditions. Area under the curve was used to compare the extent of aggregation for each condition (GraphPad Prism).

TDP-43 aggregation assay—Firstly, 0, 0.25, or 0.5 μM MBP-TEV-DDX3X or MBP-TEV-DDX3Y in buffer (200 mM NaCl, 25 mM Tris-HCl pH 8.0) was incubated in TDP-43 assay buffer (150 mM NaCl, 20 mM HEPES-NaOH pH 7.0, 1mM DTT) with 0.5 μg TEV protease for 30 minutes at room temperature. Turbidity was assessed by measuring absorbance at 395 nm in a Tecan plate reader. TDP-43 was buffer exchanged into TDP-43 assay buffer (Bio-Rad Micro Bio-Spin Chromatography Columns, following manufacturer's instructions) and concentration was determined via NanoDrop. Turbidity measurements were paused after 30 minutes in order to add 4.0 μM TDP-43 (or an equal volume of TDP-43 assay buffer) to the reaction. Then, turbidity measurements were resumed for an additional 16 hours. The data was standardized by subtracting out the initial reading at t = 1 min. from each respective condition. Values from conditions with DDX3X or DDX3Y

alone were then subtracted from the appropriate conditions with TDP-43. Area under the curve analysis was used to compare the extent of aggregation for each condition. The $t_{1/2}$ of aggregation was determined by performing a nonlinear regression (asymmetric sigmoidal) on the data starting after TDP-43 addition (t = 31 min.) (GraphPad Prism).

Protein quantification and Western blot—Protein concentrations of the samples were calculated using the Bradford Assay (Bio-Rad). Protein samples were boiled at 95°C in Laemmli sample buffer for 10 min. After brief centrifugation, the samples were loaded onto SDS-PAGE gels. After running at 180 V for 1 hr, the gels were transferred to the PVDF membranes (Millipore) by semi-dry transfer apparatus at 20 V for 50 min. Then, the PVDF membranes were blocked with 5% milk or BSA in $1 \times$ PBST for 30 mins at room temperature or 4°C overnight. The membranes were then incubated in 3% milk or BSA in $1 \times$ PBST containing the corresponding primary antibodies overnight at 4°C. After washing three times with $1 \times$ PBST, the horseradish peroxidase (HRP)-conjugated secondary antibodies (1:20,000) in 1% of milk were applied and incubated at room temperature for 1 hr. After washing three times with $1 \times$ PBST, the membranes were visualized using ECL Western Blotting Detection Kit (Thermo Fisher).

QUANTIFICATION AND STATISTICAL ANALYSIS

Images were analyzed using Fiji. All data are presented as the mean ± standard error of mean (s.e.m.) or standard deviation (s.d.) from the independent determinations. The statistical analyses were performed using the GraphPad Prism (GraphPad Software, Inc,; La Jolla, CA, USA). Differences of means were tested for statistical significance with unpaired two-tailed Student's t-test. $*p < 0.05$; $**p < 0.01$; $***p < 0.001$; $****p < 0.0001$; n.s. means $p > 0.05$.

Supplementary Material

Refer to Web version on PubMed Central for supplementary material.

ACKNOWLEDGEMENTS

REFERENCES

Ash PE, Vanderweyde TE, Youmans KL, Apicco DJ, and Wolozin B (2014). Pathological stress granules in Alzheimer's disease. Brain Res. 1584, 52–58. [PubMed: 25108040]

Baradaran-Heravi Y, Van Broeckhoven C, and van der Zee J (2020). Stress granule mediated protein aggregation and underlying gene defects in the FTD-ALS spectrum. Neurobiol. Dis. 134, 104639. [PubMed: 31626953]

Beckham C, Hilliker A, Cziko AM, Noueiry A, Ramaswami M, and Parker R (2008). The DEAD-box RNA helicase Ded1p affects and accumulates in Saccharomyces cerevisiae P-bodies. Mol. Biol. Cell 19, 984–993. [PubMed: 18162578]

Bellott DW, Hughes JF, Skaletsky H, Brown LG, Pyntikova T, Cho TJ, Koutseva N, Zaghlul S, Graves T, Rock S, et al. (2014). Mammalian Y chromosomes retain widely expressed dosage-sensitive regulators. Nature 508, 494–499. [PubMed: 24759411]

Bentmann E, Neumann M, Tahirovic S, Rodde R, Dormann D, and Haass C (2012). Requirements for stress granule recruitment of fused in sarcoma (FUS) and TAR DNA-binding protein of 43 kDa (TDP-43). J. Biol. Chem. 287, 23079–23094. [PubMed: 22563080]

Bolger AM, Lohse M, and Usadel B (2014). Trimmomatic: a flexible trimmer for Illumina sequence data. Bioinformatics 30, 2114–2120. [PubMed: 24695404]

Bryk AH, and Wisniewski JR (2017). Quantitative analysis of human red blood cell proteome. J. Proteome Res. 16, 2752–2761. [PubMed: 28689405]

Buchan JR, and Parker R (2009). Eukaryotic stress granules: the ins and outs of translation. Mol. Cell 36, 932–941. [PubMed: 20064460]

Cardinal T, Bergeron KF, Soret R, Souchkova O, Faure C, Guillon A, and Pilon N (2020). Male-biased aganglionic megacolon in the TashT mouse model of Hirschsprung disease involves upregulation of p53 protein activity and Ddx3y gene expression. PLoS Genet. 16, e1009008. [PubMed: 32898154]

Chen CY, Chan CH, Chen CM, Tsai YS, Tsai TY, Wu Lee YH, and You LR (2016). Targeted inactivation of murine Ddx3x: essential roles of Ddx3x in placentation and embryogenesis. Hum. Mol. Genet. 25, 2905–2922. [PubMed: 27179789]

Cheng W, Wang S, Zhang Z, Morgens DW, Hayes LR, Lee S, Portz B, Xie Y, Nguyen BV, Haney MS, et al. (2019). CRISPR-Cas9 screens identify the RNA helicase DDX3X as a repressor of C9ORF72 (GGGGCC)n repeat-associated non-AUG translation. Neuron 104, 885–898. [PubMed: 31587919]

Cotton AM, Price EM, Jones MJ, Balaton BP, Kobor MS, and Brown CJ (2015). Landscape of DNA methylation on the X chromosome reflects CpG density, functional chromatin state and X-chromosome inactivation. Hum. Mol. Genet. 24, 1528–1539. [PubMed: 25381334]

Ditton HJ, Zimmer J, Rajpert-De Meyts E, and Vogt PH (2004). The AZFa gene DBY (DDX3Y) is widely transcribed but the protein is limited to the male germ cells by translation control. Hum. Mol. Genet. 13, 2333–2341. [PubMed: 15294876]

Elbaum-Garfinkle S, Kim Y, Szczepaniak K, Chen CC, Eckmann CR, Myong S, and Brangwynne CP (2015). The disordered P granule protein LAF-1 drives phase separation into droplets with tunable viscosity and dynamics. Proc. Natl. Acad. Sci. U.S.A. 112, 7189–7194. [PubMed: 26015579]

Fazal FM, Han S, Parker KR, Kaewsapsak P, Xu J, Boettiger AN, Chang HY, and Ting AY (2019). Atlas of subcellular RNA localization revealed by APEX-Seq. Cell 178, 473–490. [PubMed: 31230715]

Fernandes N, Nero L, Lyons SM, Ivanov P, Mittelmeier TM, Bolger TA, and Buchan JR (2020). Stress granule assembly can facilitate but is not required for TDP-43 cytoplasmic aggregation. Biomolecules 10.

Ferretti MT, Iulita MF, Cavedo E, Chiesa PA, Schumacher Dimech A, Santuccione Chadha A, Baracchi F, Girouard H, Misoch S, Giacobini E, et al. (2018). Sex differences in Alzheimer disease - the gateway to precision medicine. Nat. Rev. Neurol. 14, 457–469. [PubMed: 29985474]

Floor SN, Condon KJ, Sharma D, Jankowsky E, and Doudna JA (2016). Autoinhibitory interdomain interactions and subfamily-specific extensions redefine the catalytic core of the human DEAD-box protein DDX3. J. Biol. Chem. 291, 2412–2421. [PubMed: 26598523]

Fujimura K, Sasaki AT, and Anderson P (2012). Selenite targets eIF4E-binding protein-1 to inhibit translation initiation and induce the assembly of non-canonical stress granules. Nucleic Acids Res. 40, 8099–8110. [PubMed: 22718973]

Gao K, Oerlemans R, and Groves MR (2020). Theory and applications of differential scanning fluorimetry in early-stage drug discovery. Biophys. Rev. 12, 85–104. [PubMed: 32006251]

Gilks N, Kedersha N, Ayodele M, Shen L, Stoecklin G, Dember LM, and Anderson P (2004). Stress granule assembly is mediated by prion-like aggregation of TIA-1. Mol. Biol. Cell 15, 5383–5398. [PubMed: 15371533]

Godfrey AK, Naqvi S, Chmatal L, Chick JM, Mitchell RN, Gygi SP, Skaletsky H, and Page DC (2020). Quantitative analysis of Y-Chromosome gene expression across 36 human tissues. Genome Res. 30, 860–873. [PubMed: 32461223]

Gozdecka M, Meduri E, Mazan M, Tzelepis K, Dudek M, Knights AJ, Pardo M, Yu L, Choudhary JS, Metzakopian E, et al. (2018). UTX-mediated enhancer and chromatin remodeling suppresses myeloid leukemogenesis through noncatalytic inverse regulation of ETS and GATA programs. Nat. Genet. 50, 883–894. [PubMed: 29736013]

Guo L, Kim HJ, Wang H, Monaghan J, Freyermuth F, Sung JC, O'Donovan K, Fare CM, Diaz Z, Singh N, et al. (2018). Nuclear-import receptors reverse aberrant phase transitions of RNA-binding proteins with prion-like domains. Cell 173, 677–692. [PubMed: 29677512]

Hallegger M, Chakrabarti AM, Lee FCY, Lee BL, Amalietti AG, Odeh HM, Copley KE, Rubien JD, Portz B, Kuret K, et al. (2021). TDP-43 condensation properties specify its RNA-binding and regulatory repertoire. Cell 184, 4680–4696. [PubMed: 34380047]

Harrison AF, and Shorter J (2017). RNA-binding proteins with prion-like domains in health and disease. Biochem. J. 474, 1417–1438. [PubMed: 28389532]

Hellenkamp B, Schmid S, Doroshenko O, Opanasyuk O, Kuhnemuth R, Rezaei Adariani S, Ambrose B, Aznauryan M, Barth A, Birkedal V, et al. (2018). Precision and accuracy of single-molecule FRET measurements-a multi-laboratory benchmark study. Nat. Methods 15, 669–676. [PubMed: 30171252]

Hondele M, Sachdev R, Heinrich S, Wang J, Vallotton P, Fontoura BMA, and Weis K (2019). DEAD-box ATPases are global regulators of phase-separated organelles. Nature 573, 144–148. [PubMed: 31435012]

Iossifov I, O'Roak BJ, Sanders SJ, Ronemus M, Krumm N, Levy D, Stessman HA, Witherspoon KT, Vives L, Patterson KE, et al. (2014). The contribution of de novo coding mutations to autism spectrum disorder. Nature 515, 216–221. [PubMed: 25363768]

Iserman C, Desroches Altamirano C, Jegers C, Friedrich U, Zarin T, Fritsch AW, Mittasch M, Domingues A, Hersemann L, Jahnel M, et al. (2020). Condensation of Ded1p promotes a translational switch from housekeeping to stress protein production. Cell 181, 818–831. [PubMed: 32359423]

Jain S, Wheeler JR, Walters RW, Agrawal A, Barsic A, and Parker R (2016). ATPase-modulated stress granules contain a diverse proteome and substructure. Cell 164, 487–498. [PubMed: 26777405]

Jamiolkowski RM, Chen C, Cooperman BS, and Goldman YE (2017). tRNA fluctuations observed on stalled ribosomes are suppressed during ongoing protein synthesis. Biophys. J. 113, 2326–2335. [PubMed: 29211986]

Joshi RN, Stadler C, Lehmann R, Lehtio J, Tegner J, Schmidt A, and Vesterlund M (2019). TcellSubC: an atlas of the subcellular proteome of human T cells. Front. Immunol. 10, 2708. [PubMed: 31849937]

Kamelgarn M, Chen J, Kuang L, Arenas A, Zhai J, Zhu H, and Gal J (2016). Proteomic analysis of FUS interacting proteins provides insights into FUS function and its role in ALS. Biochim. Biophys. Acta 1862, 2004–2014. [PubMed: 27460707]

Khalfallah Y, Kuta R, Grasmuck C, Prat A, Durham HD, and Velde CV (2018). TDP-43 regulation of stress granule dynamics in neurodegenerative disease-relevant cell types. Sci. Rep. 8.

Khong A, Matheny T, Jain S, Mitchell SF, Wheeler JR, and Parker R (2017). The stress granule transcriptome reveals principles of mRNA accumulation in stress granules. Mol. Cell. 68, 808–820. [PubMed: 29129640]

Kim D, Langmead B, and Salzberg SL (2015). HISAT: a fast spliced aligner with low memory requirements. Nat. Methods 12, 357–360. [PubMed: 25751142]

Kim TH, Tsang B, Vernon RM, Sonenberg N, Kay LE, and Forman-Kay JD (2019). Phospho-dependent phase separation of FMRP and CAPRIN1 recapitulates regulation of translation and deadenylation. Science 365, 825–829. [PubMed: 31439799]

Kim Y, and Myong S (2016). RNA remodeling activity of DEAD box proteins tuned by protein concentration, RNA length, and ATP. Mol. Cell 63, 865–876. [PubMed: 27546789]

Kimball SR, Horetsky RL, Ron D, Jefferson LS, and Harding HP (2003). Mammalian stress granules represent sites of accumulation of stalled translation initiation complexes. Am. J. Physiol. Cell Physiol. 284, C273–C284. [PubMed: 12388085]

Ku YC, Lai MH, Lo CC, Cheng YC, Qiu JT, Tarn WY, and Lai MC (2019). DDX3 Participates in Translational Control of Inflammation Induced by Infections and Injuries. Mol. Cell Biol. 39.

Lai MC, Lee YH, and Tarn WY (2008). The DEAD-box RNA helicase DDX3 associates with export messenger ribonucleoproteins as well as tip-associated protein and participates in translational control. Mol. Biol. Cell 19, 3847–3858. [PubMed: 18596238]

Lancaster AK, Nutter-Upham A, Lindquist S, and King OD (2014). PLAAC: a web and command-line application to identify proteins with prion-like amino acid composition. Bioinformatics 30, 2501–2502. [PubMed: 24825614]

Lee CS, Dias AP, Jedrychowski M, Patel AH, Hsu JL, and Reed R (2008). Human DDX3 functions in translation and interacts with the translation initiation factor eIF3. Nucleic Acids Res. 36, 4708–4718. [PubMed: 18628297]

Lennox AL, Hoye ML, Jiang R, Johnson-Kerner BL, Suit LA, Venkataramanan S, Sheehan CJ, Alsina FC, Fregeau B, Aldinger KA, et al. (2020). Pathogenic DDX3X mutations impair RNA metabolism and neurogenesis during fetal cortical development. Neuron 106, 404–420. [PubMed: 32135084]

Liao Y, Smyth GK, and Shi W (2014). featureCounts: an efficient general purpose program for assigning sequence reads to genomic features. Bioinformatics 30, 923–930. [PubMed: 24227677]

Linsalata AE, He F, Malik AM, Glineburg MR, Green KM, Natla S, Flores BN, Krans A, Archbold HC, Fedak SJ, et al. (2019). DDX3X and specific initiation factors modulate FMR1 repeat-associated non-AUG-initiated translation. EMBO Rep. 20, e47498. [PubMed: 31347257]

Love MI, Huber W, and Anders S (2014). Moderated estimation of fold change and dispersion for RNA-seq data with DESeq2. Genome Biol. 15, 550. [PubMed: 25516281]

Maharana S, Wang J, Papadopoulos DK, Richter D, Pozniakovsky A, Poser I, Bickle M, Rizk S, Guillen-Boixet J, Franzmann TM, et al. (2018). RNA buffers the phase separation behavior of prion-like RNA binding proteins. Science 360, 918–921. [PubMed: 29650702]

Manjaly ZR, Scott KM, Abhinav K, Wijesekera L, Ganesalingam J, Goldstein LH, Janssen A, Dougherty A, Willey E, Stanton BR, et al. (2010). The sex ratio in amyotrophic lateral sclerosis: A population based study. Amyotroph. Lateral Scler. 11, 439–442. [PubMed: 20225930]

Markmiller S, Soltanieh S, Server KL, Mak R, Jin W, Fang MY, Luo EC, Krach F, Yang D, Sen A, et al. (2018). Context-dependent and disease-specific diversity in protein interactions within stress granules. Cell 172, 590–604. [PubMed: 29373831]

Marmor-Kollet H, Siany A, Kedersha N, Knafo N, Rivkin N, Danino YM, Moens TG, Olender T, Sheban D, Cohen N, et al. (2020). Spatiotemporal proteomic analysis of stress granule disassembly using APEX reveals regulation by SUMOylation and links to ALS pathogenesis. Mol. Cell 80, 876–891. [PubMed: 33217318]

Mauvais-Jarvis F, Bairey Merz N, Barnes PJ, Brinton RD, Carrero JJ, DeMeo DL, De Vries GJ, Epperson CN, Govindan R, Klein SL, et al. (2020). Sex and gender: modifiers of health, disease, and medicine. Lancet 396, 565–582. [PubMed: 32828189]

McCombe PA, and Henderson RD (2010). Effects of gender in amyotrophic lateral sclerosis. Gend. Med. 7, 557–570. [PubMed: 21195356]

Mercer TR, Neph S, Dinger ME, Crawford J, Smith MA, Shearwood AM, Haugen E, Bracken CP, Rackham O, Stamatoyannopoulos JA, et al. (2011). The human mitochondrial transcriptome. Cell 146, 645–658. [PubMed: 21854988]

Meyer S, van der Meer P, van Tintelen JP, and van den Berg MP (2014). Sex differences in cardiomyopathies. Eur. J. Heart Fail 16, 238–247. [PubMed: 24464619]

Mitchell SF, Jain S, She M, and Parker R (2013). Global analysis of yeast mRNPs. Nat. Struct. Mol. Biol. 20, 127–133. [PubMed: 23222640]

Molliex A, Temirov J, Lee J, Coughlin M, Kanagaraj AP, Kim HJ, Mittag T, and Taylor JP (2015). Phase separation by low complexity domains promotes stress granule assembly and drives pathological fibrillization. Cell 163, 123–133. [PubMed: 26406374]

Moon SL, Morisaki T, Khong A, Lyon K, Parker R, and Stasevich TJ (2019). Multicolour single-molecule tracking of mRNA interactions with RNP granules. Nat. Cell Biol. 21, 162–168. [PubMed: 30664789]

Nguyen TA, Wu K, Pandey S, Lehr AW, Li Y, Bemben MA, Badger JD 2nd, Lauzon JL, Wang T, Zaghloul KA, et al. (2020). A cluster of autism-associated variants on X-linked NLGN4X functionally resemble NLGN4Y. Neuron 106, 759–768. [PubMed: 32243781]

Padron A, Iwasaki S, and Ingolia NT (2019). Proximity RNA labeling by APEX-seq reveals the organization of translation initiation complexes and repressive RNA granules. Mol. Cell 75, 875–887. [PubMed: 31442426]

Patel A, Malinovska L, Saha S, Wang J, Alberti S, Krishnan Y, and Hyman AA (2017). ATP as a biological hydrotrope. Science 356, 753–756. [PubMed: 28522535]

Patmore DM, Jassim A, Nathan E, Gilbertson RJ, Tahan D, Hoffmann N, Tong Y, Smith KS, Kanneganti TD, Suzuki H, et al. (2020). DDX3X suppresses the susceptibility of hindbrain lineages to medulloblastoma. Dev. Cell 54, 455–470. [PubMed: 32553121]

Phung B, Ciesla M, Sanna A, Guzzi N, Beneventi G, Cao Thi Ngoc P, Lauss M, Cabrita R, Cordero E, Bosch A, et al. (2019). The X-linked DDX3X RNA helicase dictates translation reprogramming and metastasis in melanoma. Cell Rep. 27, 3573–3586. [PubMed: 31216476]

Portz B, Lee BL, and Shorter J (2021). FUS and TDP-43 phases in health and disease. Trends Biochem. Sci. 46, 550–563. [PubMed: 33446423]

Protter DSW, and Parker R (2016). Principles and properties of stress granules. Trends Cell Biol. 26, 668–679. [PubMed: 27289443]

Qamar S, Wang GZ, Randle SJ, Ruggeri FS, Varela JA, Lin JQ, Phillips EC, Miyashita A, Williams D, Strohl F, et al. (2018). FUS phase separation is modulated by a molecular chaperone and methylation of arginine cation-pi interactions. Cell 173, 720–734. [PubMed: 29677515]

Robert X, and Gouet P (2014). Deciphering key features in protein structures with the new ENDscript server. Nucleic Acids Res. 42, W320–324. [PubMed: 24753421]

Ruzzo EK, Perez-Cano L, Jung JY, Wang LK, Kashef-Haghighi D, Hartl C, Singh C, Xu J, Hoekstra JN, Leventhal O, et al. (2019). Inherited and de novo genetic risk for autism impacts shared networks. Cell 178, 850–866. [PubMed: 31398340]

Saito M, Hess D, Eglinger J, Fritsch AW, Kreysing M, Weinert BT, Choudhary C, and Matthias P (2019). Acetylation of intrinsically disordered regions regulates phase separation. Nat. Chem. Biol. 15, 51–61. [PubMed: 30531905]

Scala M, Torella A, Severino M, Morana G, Castello R, Accogli A, Verrico A, Vari MS, Cappuccio G, Pinelli M, et al. (2019). Three de novo DDX3X variants associated with distinctive brain developmental abnormalities and brain tumor in intellectually disabled females. Eur. J. Hum. Genet. 27, 1254–1259. [PubMed: 30936465]

Schindelin J, Arganda-Carreras I, Frise E, Kaynig V, Longair M, Pietzsch T, Preibisch S, Rueden C, Saalfeld S, Schmid B, et al. (2012). Fiji: an open-source platform for biological-image analysis. Nat. Methods 9, 676–682. [PubMed: 22743772]

Schneider JW, Oommen S, Qureshi MY, Goetsch SC, Pease DR, Sundsbak RS, Guo W, Sun M, Sun H, Kuroyanagi H, et al. (2020). Dysregulated ribonucleoprotein granules promote cardiomyopathy in RBM20 gene-edited pigs. Nat. Med. 26, 1788–1800. [PubMed: 33188278]

Schuster BS, Dignon GL, Tang WS, Kelley FM, Ranganath AK, Jahnke CN, Simpkins AG, Regy RM, Hammer DA, Good MC, et al. (2020). Identifying sequence perturbations to an intrinsically disordered protein that determine its phase-separation behavior. Proc. Natl. Acad. Sci. U.S.A. 117, 11421–11431. [PubMed: 32393642]

Sharma D, and Jankowsky E (2014). The Ded1/DDX3 subfamily of DEAD-box RNA helicases. Crit. Rev. Biochem. Mol. 49, 343–360.

Shi B, Li W, Song YS, Wang ZJ, Ju R, Ulman A, Hu J, Palomba F, Zhao YF, Le JP, et al. (2021). UTX condensation underlies its tumour-suppressive activity. Nature 597, 726–731. [PubMed: 34526716]

Shih JW, Wang WT, Tsai TY, Kuo CY, Li HK, and Wu Lee YH (2012). Critical roles of RNA helicase DDX3 and its interactions with eIF4E/PABP1 in stress granule assembly and stress response. Biochem. J. 441, 119–129. [PubMed: 21883093]

Silva JM, Rodrigues S, Sampaio-Marques B, Gomes P, Neves-Carvalho A, Dioli C, Soares-Cunha C, Mazuik BF, Takashima A, Ludovico P, et al. (2019). Dysregulation of autophagy and stress granule-related proteins in stress-driven Tau pathology. Cell Death Differ. 26, 1411–1427. [PubMed: 30442948]

Snijders Blok L, Madsen E, Juusola J, Gilissen C, Baralle D, Reijnders MR, Venselaar H, Helsmoortel C, Cho MT, Hoischen A, et al. (2015). Mutations in DDX3X are a common cause of unexplained intellectual disability with gender-specific effects on Wnt signaling. Am. J. Hum. Genet. 97, 343–352. [PubMed: 26235985]

Song H, and Ji X (2019). The mechanism of RNA duplex recognition and unwinding by DEAD-box helicase DDX3X. Nat. Commun. 10, 3085. [PubMed: 31300642]

Soto-Rifo R, Rubilar PS, Limousin T, de Breyne S, Decimo D, and Ohlmann T (2012). DEAD-box protein DDX3 associates with eIF4F to promote translation of selected mRNAs. EMBO J. 31, 3745–3756. [PubMed: 22872150]

Sun Z, Diaz Z, Fang X, Hart MP, Chesi A, Shorter J, and Gitler AD (2011). Molecular determinants and genetic modifiers of aggregation and toxicity for the ALS disease protein FUS/TLS. PLoS Biol. 9, e1000614. [PubMed: 21541367]

Szaflarski W, Fay MM, Kedersha N, Zabel M, Anderson P, and Ivanov P (2016). Vinca alkaloid drugs promote stress-induced translational repression and stress granule formation. Oncotarget 7, 30307–30322. [PubMed: 27083003]

Szappanos D, Tschismarov R, Perlot T, Westermayer S, Fischer K, Platanitis E, Kallinger F, Novatchkova M, Lassnig C, Muller M, et al. (2018). The RNA helicase DDX3X is an essential mediator of innate antimicrobial immunity. Plos Pathog. 14, e1007397. [PubMed: 30475900]

Tan RH, Ke YD, Ittner LM, and Halliday GM (2017). ALS/FTLD: experimental models and reality. Acta Neuropathol. 133, 177–196. [PubMed: 28058507]

Tauber D, Tauber G, Khong A, Van Treeck B, Pelletier J, and Parker R (2020). Modulation of RNA condensation by the DEAD-box protein eIF4A. Cell 180, 411–426. [PubMed: 31928844]

Vakilian H, Mirzaei M, Tabar MS, Pooyan P, Rezaee LH, Parker L, Haynes PA, Gourabi H, Baharvand H, and Salekdeh GH (2015). DDX3Y, a male-specific region of Y chromosome gene, may modulate neuronal differentiation. J. Proteome Res. 14, 3474–3483. [PubMed: 26144214]

Valentin-Vega YA, Wang YD, Parker M, Patmore DM, Kanagaraj A, Moore J, Rusch M, Finkelstein D, Ellison DW, Gilbertson RJ, et al. (2016). Cancer-associated DDX3X mutations drive stress granule assembly and impair global translation. Sci. Rep. 6, 25996. [PubMed: 27180681]

Venkataramanan S, Gadek M, Calviello L, Wilkins K, and Floor SN (2021). DDX3X and DDX3Y are redundant in protein synthesis. RNA 27, 1577–1588. [PubMed: 34535544]

Vernon RM, Chong PA, Tsang B, Kim TH, Bah A, Farber P, Lin H, and Forman-Kay JD (2018). Pi-Pi contacts are an overlooked protein feature relevant to phase separation. Elife 7, e31486. [PubMed: 29424691]

Walker IH, Hsieh PC, and Riggs PD (2010). Mutations in maltose-binding protein that alter affinity and solubility properties. Appl. Microbiol. Biotechnol. 88, 187–197. [PubMed: 20535468]

Wang J, Choi JM, Holehouse AS, Lee HO, Zhang X, Jahnel M, Maharana S, Lemaitre R, Pozniakovsky A, Drechsel D, et al. (2018a). A molecular grammar governing the driving forces for phase separation of prion-like RNA binding proteins. Cell 174, 688–699. [PubMed: 29961577]

Wang X, Posey JE, Rosenfeld JA, Bacino CA, Scaglia F, Immken L, Harris JM, Hickey SE, Mosher TM, Slavotinek A, et al. (2018b). Phenotypic expansion in DDX3X - a common cause of intellectual disability in females. Ann. Clin. Transl. Neurol. 5, 1277–1285. [PubMed: 30349862]

Watkins J, Ghosh A, Keerie AFA, Alix JJP, Mead RJ, and Sreedharan J (2020). Female sex mitigates motor and behavioural phenotypes in TDP-43(Q331K) knock-in mice. Sci. Rep. 10, 19220. [PubMed: 33154447]

Wu T, Yu J, Gale-Day Z, Woo A, Suresh A, Hornsby M, and Gestwicki JE (2020). Three essential resources to improve differential scanning fluorimetry (DSF) experiments. bioRxiv.

Xue B, Dunbrack RL, Williams RW, Dunker AK, and Uversky VN (2010). PONDR-FIT: a meta-predictor of intrinsically disordered amino acids. Biochim. Biophys. Acta. 1804, 996–1010. [PubMed: 20100603]

Yedavalli VSRK, Neuveut C, Chi YH, Kleiman L, and Jeang KT (2004). Requirement of DDX3 DEAD box RNA helicase for HIV-1 Rev-RRE export function. Cell 119, 381–392. [PubMed: 15507209]

Zhou Y, Zhou B, Pache L, Chang M, Khodabakhshi AH, Tanaseichuk O, Benner C, and Chanda SK (2019). Metascape provides a biologist-oriented resource for the analysis of systems-level datasets. Nat. Commun. 10, 1523. [PubMed: 30944313]

Highlights:

- The N-terminal IDR of DDX3Y more strongly promotes condensation than DDX3X.

- Slower ATPase activity of DDX3Y contributes to weaker dissolution of condensates.

- Stronger phase separation of DDX3Y than DDX3X leads to more translation repression.

- DDX3Y condensates enhance aggregation of FUS more strongly than DDX3X.
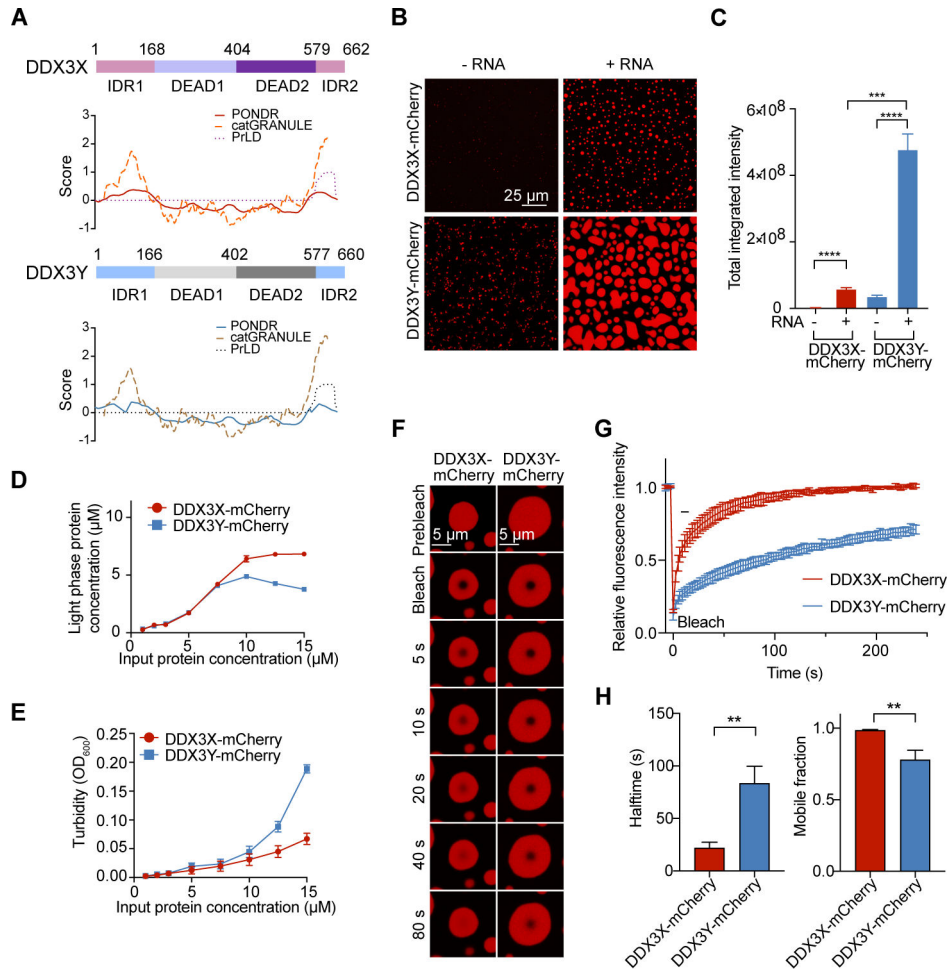
Figure 1. DDX3Y has a stronger LLPS propensity compared to DDX3X *in vitro*.

(A) Structural prediction of DDX3X and DDX3Y using PONDR (natural disordered regions), PLAAC (prion-like amino acid regions), and catGRANULE (LLPS propensity).

(B) *In vitro* droplet formation of 10 μM recombinant DDX3X-mCherry or DDX3Y-mCherry in the absence or presence of 200 ng/μL poly(U)-RNA. Scale bar, 25 μm.

(C) Quantification of the total integrated intensity of DDX3X condensation and DDX3Y condensation in Figure 1B. A two-tailed t-test was used to calculate the *p*-value. ***$p <$ 0.001, **** $p < 0.0001$.

(D) Concentrations of DDX3 proteins in the light phase (supernatant after centrifugation) *vs.* input protein concentrations.

(E) Turbidity (absorbance at 600 nm) of DDX3X-mCherry and DDX3Y-mCherry LLPS. The mean value of turbidity and protein concentration for each condition from three separate protein purifications and three technical repeats were plotted in Figure 1D and 1E.

(F) Time-lapse images of *in vitro* FRAP experiments. The FRAP experiments were performed identically for DDX3X-mCherry and DDX3Y-mCherry droplets.

(G) FRAP curves for *in vitro* droplets of DDX3X-mCherry (red) and DDX3Y-mCherry (blue). The traces of the FRAP data represent mean ± s.e.m (n = 3, from three independent experiments).
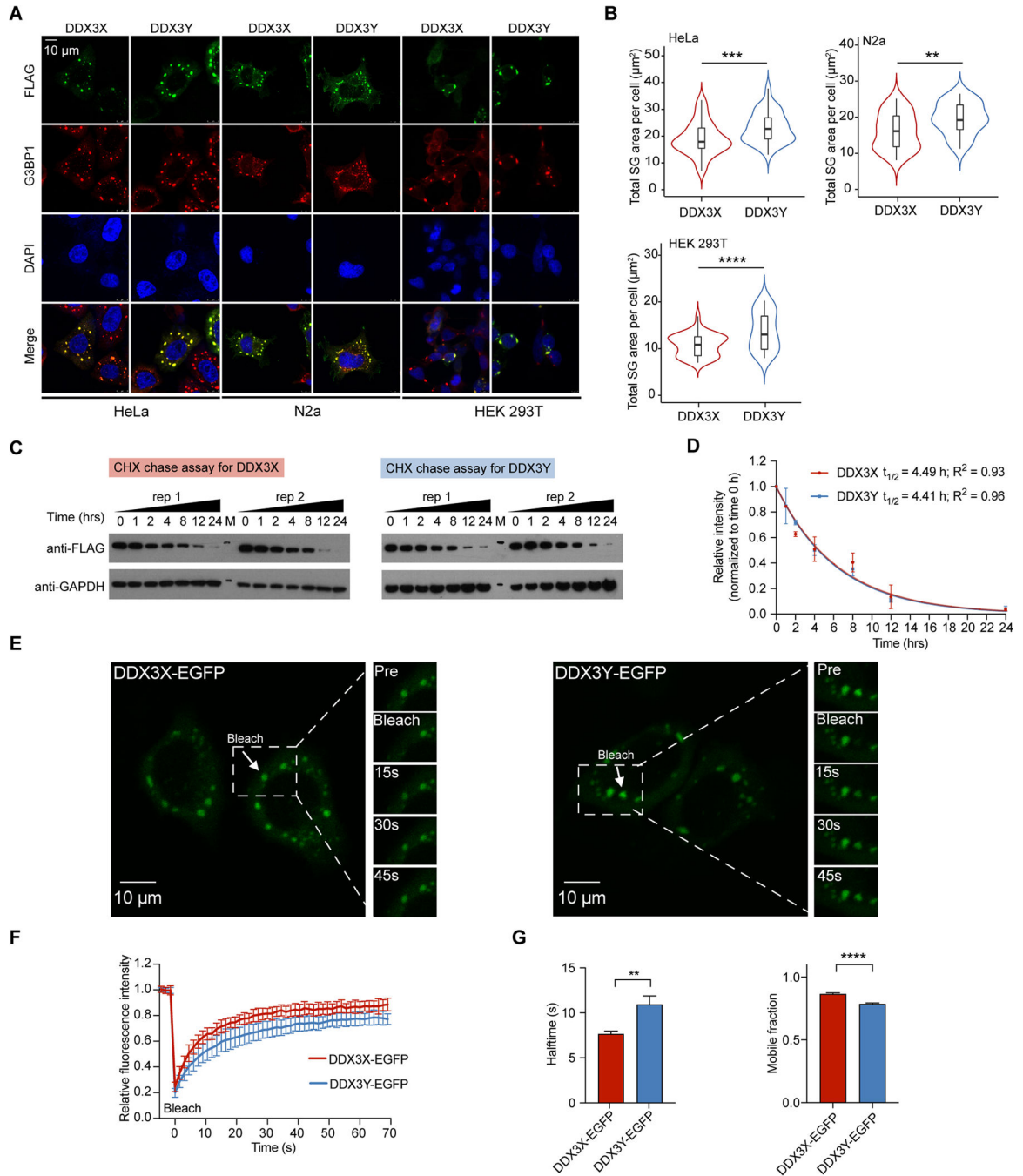
(H) Halftime and mobile fractions from Figure 1G. A two-tailed t-test was used to calculate the *p*-value. **$p < 0.01$.

See also Figure S1.

Figure 2. DDX3Y has a stronger LLPS propensity compared to DDX3X in cells.

(A) Representative images of co-localization of DDX3X and DDX3Y with G3BP1 in HeLa, N2a, and HEK 293T cells with the endogenous DDX3X knocked down upon arsenite treatment (500 μM, 1 hr). Scale bar, 10 μm.

(B) Violin plots of the total SG area of DDX3X- or DDX3Y-positive SGs per cell across 50 cells upon arsenite treatment (500 μM, 1 hr) in endogenous DDX3X-depleted HeLa, N2a, or HEK 293T cells (n = 50 cells in total, from 3 biologically independent experiments). p values were determined by a two-tailed t-test; **$p < 0.01$, ***$p < 0.001$, **** $p < 0.0001$.

(C) Cycloheximide (CHX) chase assay to determine the cellular half-life of DDX3X and DDX3Y in HeLa cells. Two biological replicates for DDX3X and for DDX3Y were performed. "M" represents the protein ladder on the Western blot membranes (markers: upper 75 kDa, lower 37 kDa).

(D) Quantification of the protein levels in Figure 2C. The intensity of each DDX3X and DDX3Y band was normalized to the corresponding GAPDH intensity before being normalized to the intensity at the corresponding 0 hr time point. The half-lives of DDX3X and DDX3Y were 4.49 hrs and 4.41 hrs, respectively.

(E) Time-lapse images of photobleached SGs in HeLa cells expressing DDX3X-EGFP (left) or DDX3Y-EGFP (right) from in-cell FRAP experiments. The photobleaching events and fluorescence recovery by DDX3X-EGFP- and DDX3Y-EGFP-positive SGs are highlighted by the arrow in each outlined box.

(F) FRAP curves for DDX3X-EGFP (red) and DDX3Y-EGFP (blue) in HeLa cells. The trace of the FRAP data represents mean ± s.e.m. (n = 20 independent measurements, from 3 biologically independent experiments).

(G) The halftime and mobile fractions in Figure 2E & 2F. A two-tailed t-test was used to calculate the p-value. $**p < 0.01$, $****\ p < 0.0001$.

See also Figure S2.
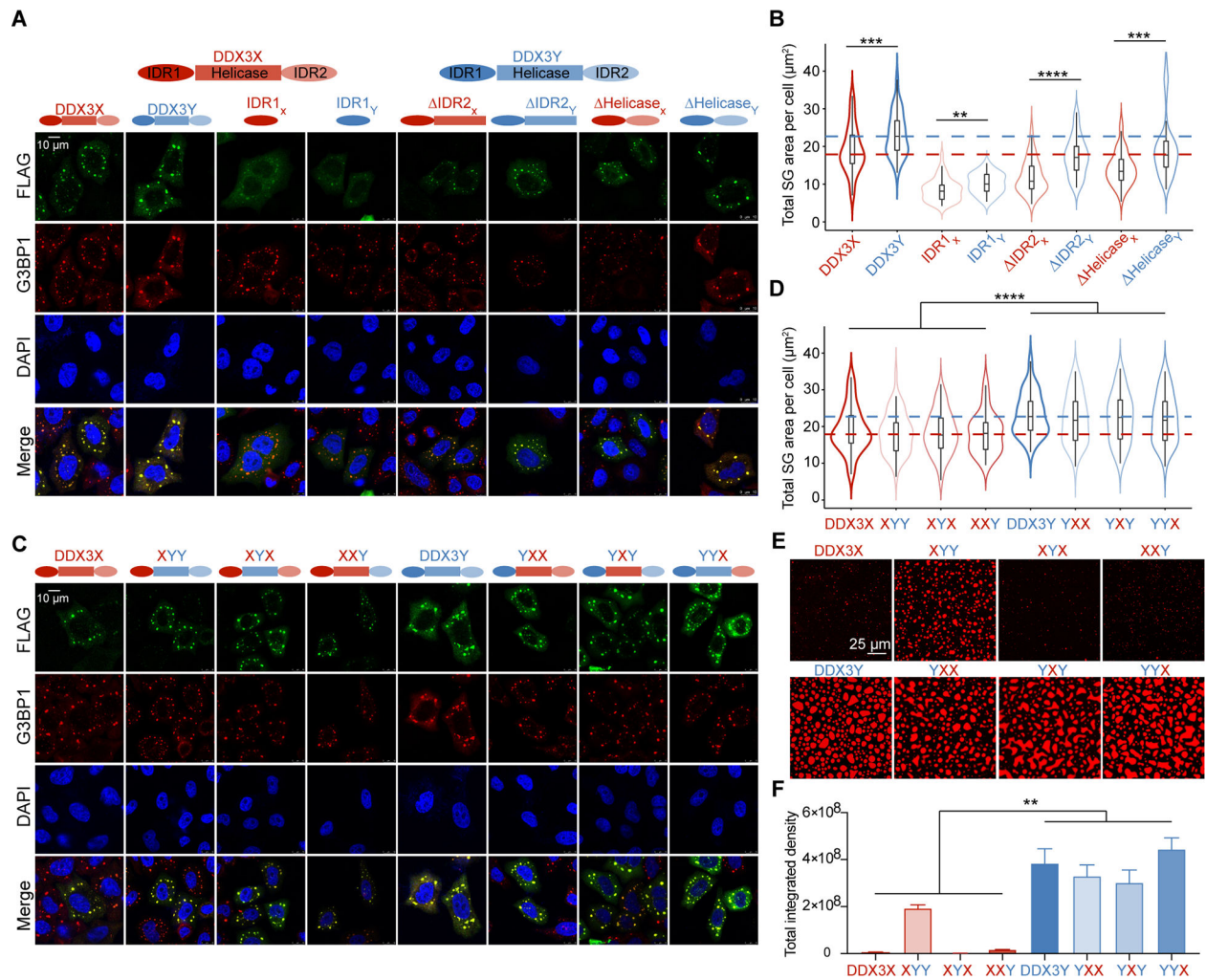
Figure 3. IDR1 of DDX3Y more strongly promotes phase separation than IDR1 of DDX3X.

(A) Co-localization of DDX3X or DDX3Y domain truncation variants in HeLa cells with G3BP1 upon 500 μM arsenite treatment for 1 hr. Scale bar, 10 μm.

(B) Violin plots of the total SG area of truncation SGs per cell (n = 50 cells in total, from three biologically independent experiments). The median of the total SG areas per cell of wild-type DDX3X-SGs and DDX3Y-SGs are indicated by red and blue dashed lines, respectively. p values were determined by a two-tailed t-test; $**p < 0.01$, $***p < 0.001$, $****p < 0.0001$.

(C) Co-localization of DDX3X or DDX3Y domain swap variants in HeLa cells with G3BP1 upon 500 μM arsenite treatment for 1 hr. Scale bar, 10 μm.

(D) Violin plots of the total SG area of DDX3X or DDX3Y domain swap SGs per cell (50 cells in total from three biologically independent experiments). The median sum of SG areas per cell of wild-type DDX3X-SGs and DDX3Y-SGs is indicated by red and blue dashed lines, respectively. p values were determined by nested t-test to compare all domain-swapped variants with X^{IDR1} versus all domain-swapped variants with Y^{IDR1}; $****p < 0.0001$.

(E) *In vitro* droplet formation of 7.5 μM recombinant DDX3X-mCherry, DDX3Y-mCherry, or domain swap variants of DDX3X and DDX3Y in the presence of 200 ng/μL poly(U)-RNA. Scale bar, 25 μm.

(F) Quantification of the total integrated intensity of the different conditions shown in Figure 3E. Error bars represent s.d. from three repeats at each condition. *p* values were determined by nested t-test to compare all domain-swapped variants with X^{IDR1} versus all domain-swapped variants with Y^{IDR1}; $**p < 0.01$.

See also Figure S3.
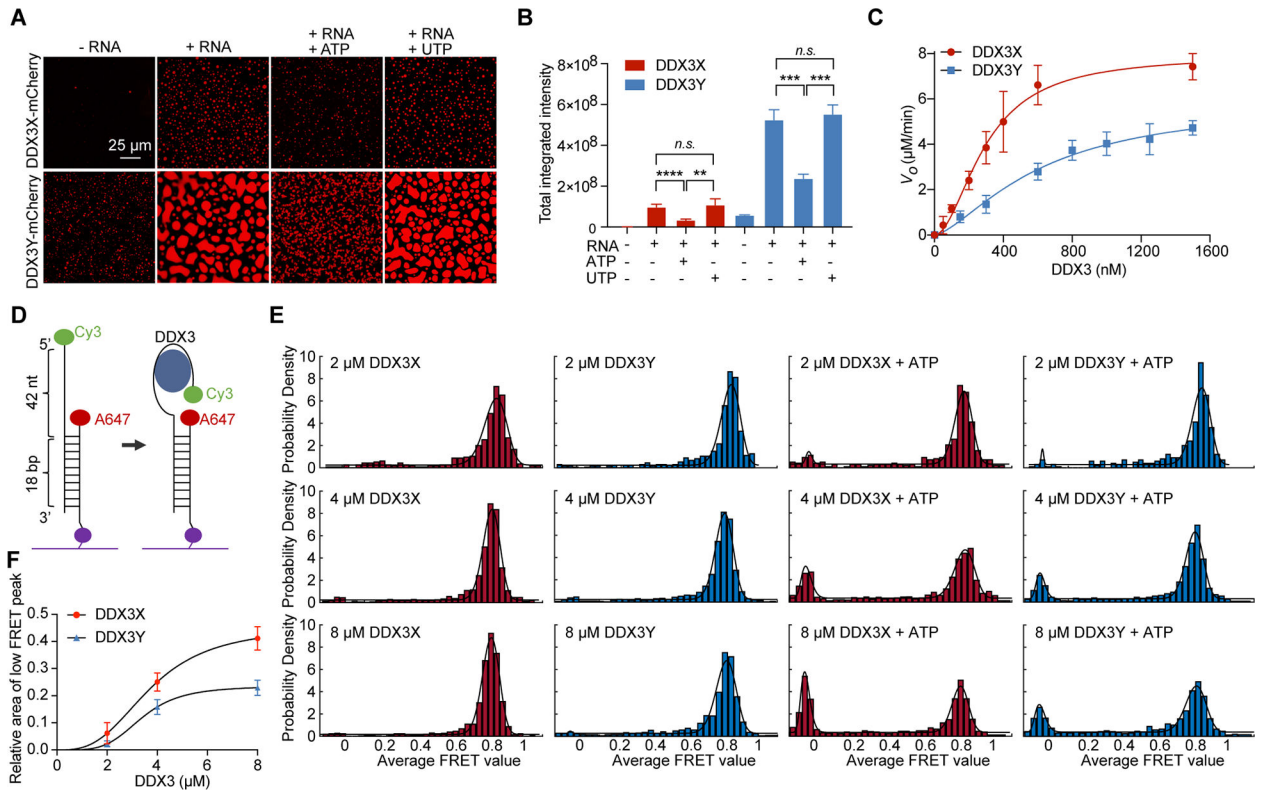
Figure 4. The weaker ATPase activity of DDX3Y compared to DDX3X weakens its condensate disassembly.

A) *In vitro* droplet formation of 10 μM recombinant DDX3X-mCherry and DDX3Y-mCherry in the absence and presence of 200 ng/μL poly(U)-RNA with and without the addition of 4 mM ATP or UTP. Scale bar, 25 μm.

(B) Quantification of the total integrated intensity of different groups of condensates shown in Figure 4A. A two-tailed t-test was used to calculate the *p*-value. *n.s.* means $p > 0.05$, **$p < 0.01$, ***$p < 0.001$, and **** $p < 0.0001$.

(C) ATPase activity of DDX3X and DDX3Y, as measured by release of free phosphate, in μM/min. Error bars represent ± s.d. from 6 individual replicates. The background value (initial rate when no protein was added) was subtracted from each point before plotting and curve fitting to the Hill equation. DDX3X: $V_{max} = 7.9 \pm 0.4$ μM/min, H = 1.9 ± 0.2, $K_{1/2} = 297.2 \pm 22.6$ nM. DDX3Y: $V_{max} = 5.9 \pm 0.7$ μM/min, H = 1.5 ± 0.2, $K_{1/2} = 617.9 \pm 123.6$ nM. All fitting parameter uncertainties are ± s.e.m.

(D) Schematic of smFRET RNA probe.

(E) FRET efficiency distributions with increasing protein concentrations (2, 4, and 8 μM) of DDX3X and DDX3Y in the presence or absence of ATP. FRET values were collected from over 1000 molecules to build the histograms.

(F) Fitting of the Hill equation to relative values of the low FRET peak area (with background subtracted) in Figure 4E for DDX3X and DDX3Y.

See also Figure S4.
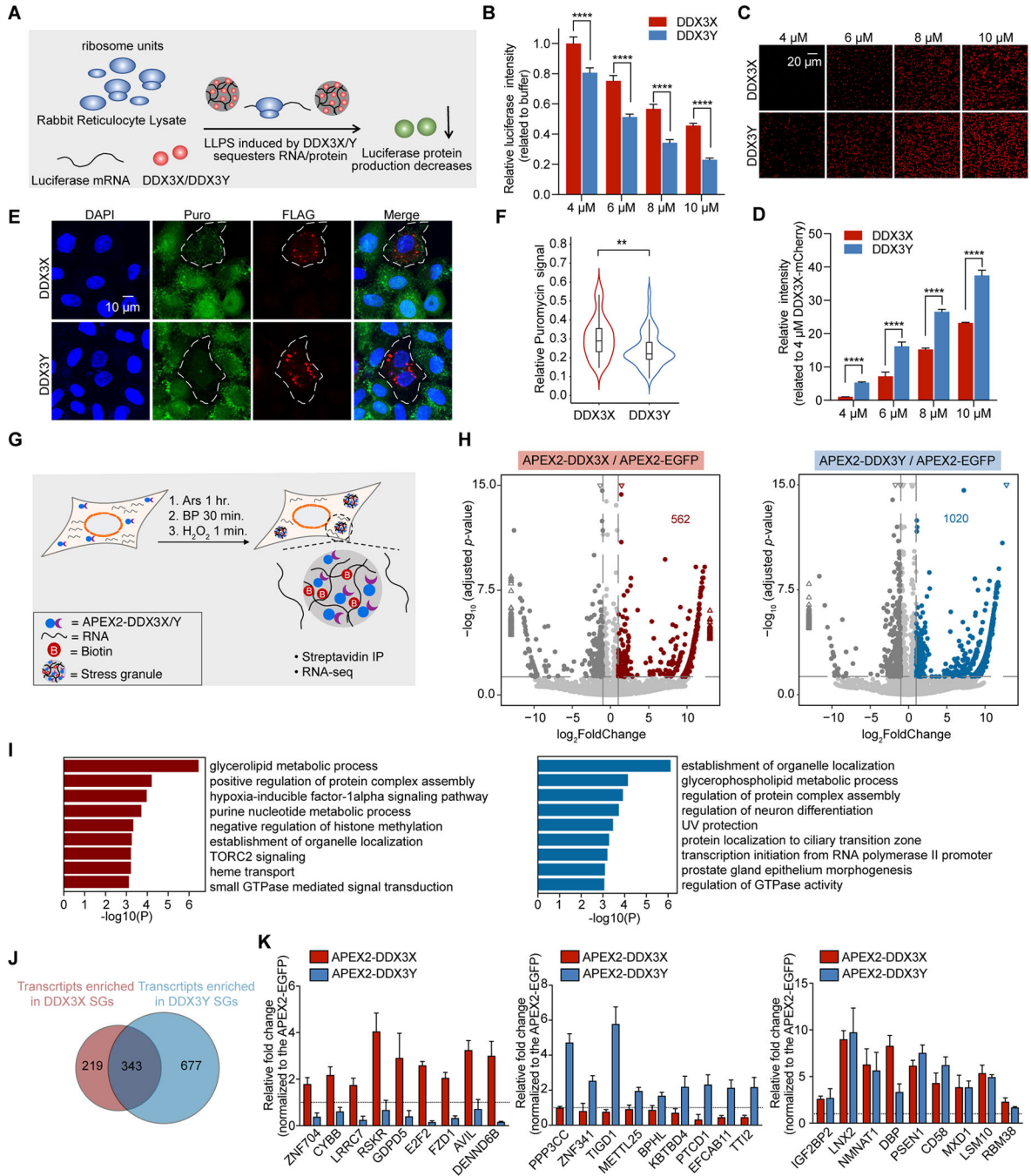
Figure 5. DDX3X and DDX3Y condensation inhibit the translation of luciferase RNA, and DDX3X- and DDX3Y-positive SGs have shared and unique RNA constituents in cells.

(A) Schematic illustration of the *in vitro* translation assay.

(B) *In vitro* translation inhibition at the indicated concentrations of DDX3X-mCherry or DDX3Y-mCherry. *p* values were determined by two-tailed t-test; ****p < 0.0001.

(C) DDX3X-mCherry and DDX3Y-mCherry phase separation in the reticulocyte assay at each indicated concentration; scale bar, 20 μm.

(D) Quantification of the total integrated intensity of different condensates shown in Figure 5C.

(E) Puromycin incorporation assay to determine the extent of translation repression in cells with DDX3X-positive SGs and DDX3Y-positive SGs. The white outlines indicate the cells which express exogenous DDX3X or DDX3Y.

(F) Quantification of puromycin signal in Figure 5E. Only cells expressing exogenous DDX3X or DDX3Y were selected, and the total puromycin signal in each cell was quantified. The total puromycin signals in neighboring cells not expressing exogenous DDX3X or DDX3Y were quantified similarly and used to normalize the data. p-value was determined by two-tailed t-test; $**p < 0.01$.

(G) Schematic illustration of APEX2-mediated proximity labeling reaction.

(H) Volcano plots showing differential RNA enrichment in streptavidin pull-downs from APEX2-DDX3X (left) and APEX2-DDX3Y (right) expressing cells compared to APEX2-EGFP expressing cells after 500 μM arsenite treatment for 1 hr. Differentially expressed genes are shown in red and blue for APEX2-DDX3X-enriched and APEX2-DDX3Y-enriched RNAs respectively (adjusted $p < 0.05$, $\log_2$ fold change > 1) and dark gray for APEX2-DDX3X-depleted and APEX2-DDX3Y-depleted RNAs (adjusted $p < 0.05$, $\log_2$ fold change < -1). The rest of the RNAs are shown in light gray for both DDX3X and DDX3Y. The triangles represent the transcripts with $\log_2$ fold change > 13 or $\log_2$ fold change < -13 in the X-axis; $-\log_{10}$ adjusted $p > 15$ in the Y-axis.

(I) Gene Ontology (GO) analysis of the differentially enriched RNA groups in Figure 5E; red: APEX2-DDX3X-enriched RNAs; and blue: APEX2-DDX3Y-enriched mRNAs.

(J) Venn diagram quantifying the overlapping and distinct RNA clients enriched by APEX2-DDX3X and APEX2-DDX3Y after arsenite treatment.

(K) Relative fold change of select RNAs used to conduct RT-qPCR validation of the sequencing results.

See also Figure S5.
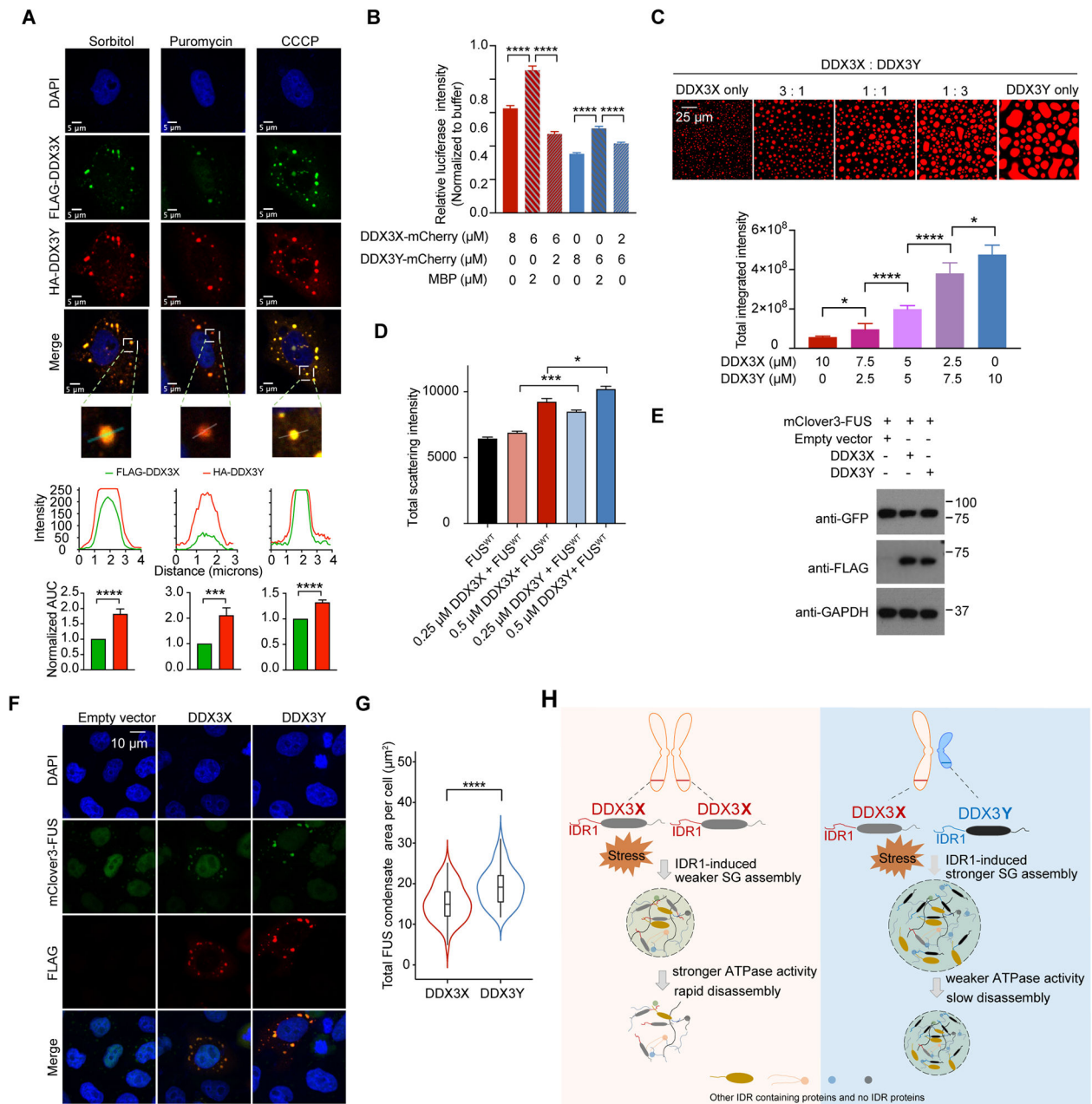
Figure 6. A combination of DDX3X and DDX3Y shows a stronger propensity of LLPS and translation repression than DDX3X alone; and DDX3Y enhances FUS aggregation and accelerates TDP-43 aggregation more than DDX3X.

(A) Immunofluorescence images of SGs containing both FLAG-DDX3X and HA-DDX3Y in HeLa cells treated with sorbitol, puromycin, or CCCP. Below each image, traces of fluorescence intensity profiles through positions denoted by the white lines in the merged images. The area under the curve (AUC) normalized to that of FLAG-DDX3X is plotted for each intensity profile and shows that the signal from HA-DDX3Y is consistently higher than the signal from FLAG-DDX3X.

(B) A mixture of DDX3X-mCherry and DDX3Y-mCherry at the annotated concentrations differentially repress *in vitro* translation of luciferase RNA. Overall, DDX3Y represses

translation more than DDX3X. *p* values were determined by two-tailed t-test; ****p < 0.0001.

(C) *In vitro* droplet formation of recombinant DDX3X-mCherry and DDX3Y-mCherry at the annotated ratios in the presence of 200 ng/µL poly(U)-RNA (top panel). Scale bar, 25 µm. Quantification of the total integrated intensity of each type of condensate (bottom panel). *p* values were determined by two-tailed t-test; *p < 0.05, ****p < 0.0001.

(D) DDX3Y more strongly promotes FUS aggregation than DDX3X *in vitro*. The area under the curve for each time course of light scattering at 395 nm in Figure S6E was used to compare the extent of aggregation for each condition. *p* values were determined by two-tailed t-test; *p < 0.05, ***p < 0.001.

(E) Western blots showing the expression of DDX3X and DDX3Y in DOX-inducible stable cell lines expressing mClover3-FUS.

(F) Representative images showing the localization of Flag-DDX3X, Flag-DDX3Y, and mClover-FUS upon arsenite treatment (500 µm, 1 hr). Scale bar, 10 µm.

(G) The total area of granules containing mClover3-FUS and Flag-DDX3X or granules containing mClover3-FUS and Flag-DDX3Y per cell was quantified (n = 50 cells in total, from three biologically independent experiments). *p* values were determined by a two-tailed t-test; ****p < 0.0001.

(H) Schematic illustration of how sexually dimorphic RNA helicases DDX3X and DDX3Y differentially regulate RNA translation through phase separation.

See also Figure S6.

Key resources table

REAGENT or RESOURCE	SOURCE	IDENTIFIER
Antibodies		
Rabbit polyclonal anti-G3BP1	Proteintech	Cat# 13057-2-AP, RRID:AB_2232034
Rabbit polyclonal anti-HA	Abcam	Cat# ab9110, RRID:AB_307019
Mouse monoclonal anti-FLAG	Sigma-Aldrich	Cat# F3165, RRID:AB_259529
Rat monoclonal anti-FLAG	Invitrogen	Cat# MA1-142, RRID:AB_2536846
HRP conjugated anti-FLAG	Invitrogen	Cat# MA1-91878-HRP, RRID:AB_2537626
Rabbit polyclonal anti-GAPDH	Invitrogen	Cat# PA1-16777, RRID:AB_568552
Mouse monoclonal anti-GFP	Santa Cruz	Cat# sc-996, RRID:AB_2187785
Mouse anti-puromycin, clone 12D10, Alexa Fluor 488 conjugated antibody	Sigma-Aldrich	Cat# MABE343-AF488, RRID:AB_2736875
Goat anti-mouse IgG (H&L) (HRP)	Abcam	Cat# ab6789, RRID:AB_955439
Mouse monoclonal anti-ATP5A	Abcam	Cat# ab14748, RRID:AB_301447
Goat anti-Mouse IgG H&L (Alex Fluor® 647)	Abcam	Cat# ab150115, RRID:AB_2687948
Goat anti-Rabbit IgG H&L (Alexa Fluor® 594)	Abcam	Cat# ab150080, RRID:AB_2650602
Goat anti-Mouse IgG H&L (Alexa Fluor® 488)	Abcam	Cat# ab150113, RRID:AB_2576208
Goat Anti-Rat IgG H&L (Alexa Fluor® 488)	Abcam	Cat# ab150157, RRID:AB_2722511
Mouse monoclonal anti-DDX3	Abcam	Cat# ab196032
Rabbit polyclonal anti-DDX3Y	Invitrogen	Cat# PA5-90055, RRID:AB_2805908
Bacterial and Virus Strains		
One Shot™ TOP10 Chemically Competent *E. coli*	Invitrogen	Cat# 404003
BL21(DE3)-RIL Competent *E. coli*	Agilent	Cat# 230204
Chemicals, Peptides, and Recombinant Proteins		
Streptavidin-HRP	Cell Signaling Technology	Cat# 3999, RRID:AB_10830897
DDX3X-mCherry recombinant protein	This paper	N/A
DDX3Y-mCherry recombinant protein	This paper	N/A
MBP-DDX3X recombinant protein	This paper	N/A
MBP-DDX3Y recombinant protein	This paper	N/A
N-Lauroylsarcosine sodium salt solution	Sigma-Aldrich	Cat# L7414-10ML
SUPERase·In™ RNase Inhibitor	Invitrogen	Cat# AM2694
Proteinase K solution (20 mg/mL)	Life Technologies	Cat# AM2548
Lipofectamine 2000	Thermo Fisher	Cat# 11668019
Pierce streptavidin magnetic beads	Thermo Fisher	Cat# 88816
Agencourt AMPure XP	Beckman Coulter	Cat# A63881
TRIzol	Invitrogen	Cat# 15596026
IPTG	Thermo Fisher	Cat# 34060
DAPI	Sigma-Aldrich	Cat# D9542
Fisher BioReagents™ Bovine Serum Albumin, Heat Shock Treated	Fisher Scientific	Cat# BP1600-100

REAGENT or RESOURCE	SOURCE	IDENTIFIER
Polyuridylic acid potassium salt	Sigma-Aldrich	Cat# P9528-10MG
Sodium arsenite	Spectrum Chemical	Cat# S-222
Sorbitol solution	Spectrum Chemical	Cat# S-1525
Thapsigargin	ACROS Organics	Cat# AC328570010
CCCP	Alfa Aesar	Cat# AAL06932MC
Puromycin	Takara Bio USA	Cat# 631305
MG132	Sigma-Aldrich	Cat# 474790-1 MG
Hydrogen peroxide solution	Sigma-Aldrich	Cat# H1009
Biotin-phenol	Iris Biotech	Cat# LS-3500.1000
Sodium azide	Sigma-Aldrich	Cat# S2002
Sodium ascorbate	Sigma-Aldrich	Cat# A7631
Trolox	Sigma-Aldrich	Cat# 238813
Cycloheximide	Sigma-Aldrich	Cat# C7698
Critical Commercial Assays		
Malachite Green Phosphate Assay Kit	Sigma-Aldrich	Cat# MAK307-1KT
Flexi® Rabbit Reticulocyte Lysate System	Promega	Cat# L4540
Luna® Universal One-Step RT-qPCR Kit	NEB	Cat# M3005L
Truseq Stranded mRNA Library Prep	Illumina	Cat# 20020594
Dynabeads™ mRNA Purification Kit (for mRNA purification from total RNA preps)	Invitrogen	Cat# 61006
EnzChek™ Phosphate Assay Kit	Thermo Fisher	Cat# E6646
RNA Clean and Concentrator-5	Zymo Research	Cat# R1016
Deposited Data		
APEX-seq with stress treatment	This paper	GEO: GSE171792
APEX-seq without stress treatment	This paper	GEO: GSE193783
Raw data	This paper; Mendeley Data	https://dx.doi.org/10.17632/9hs5d4fvgd.1
Experimental Models: Cell Lines		
Human: HeLa	ATCC	CCL-2, RRID:CVCL_0030
Human: HEK 293T	ATCC	CRL-3216, RRID:CVCL_0063
Mouse: N2a	ATCC	CCL-131, RRID:CVCL_0470
Oligonucleotides		
Primers for all the recombinant DNA	This paper	Table S3
Recombinant DNA		
pPB DDX3X	This paper	N/A
pPB DDX3Y	This paper	N/A
pPB DDX3X-IDR1	This paper	N/A
pPB DDX3Y-IDR1	This paper	N/A
pPB DDX3X-Helicae	This paper	N/A
pPB DDX3Y-Helicae	This paper	N/A
pPB DDX3X-IDR2	This paper	N/A

REAGENT or RESOURCE	SOURCE	IDENTIFIER
pPB DDX3Y-IDR2	This paper	N/A
pPB DDX3X- IDR1	This paper	N/A
pPB DDX3Y- IDR1	This paper	N/A
pPB DDX3X- IDR2	This paper	N/A
pPB DDX3Y- IDR2	This paper	N/A
pPB DDX3X- Helicase	This paper	N/A
pPB DDX3Y- Helicase	This paper	N/A
pPB DDX3X^{IDR1}-DDX3Y^{Helicae}-DDX3Y^{IDR2}	This paper	N/A
pPB DDX3Y^{IDR1}-DDX3X^{Helicae}-DDX3X^{IDR2}	This paper	N/A
pPB DDX3X^{IDR1}-DDX3X^{helicae}-DDX3Y^{IDR2}	This paper	N/A
pPB DDX3Y^{IDR1}-DDX3Y^{helicae}-DDX3X^{IDR2}	This paper	N/A
pPB DDX3X^{IDR1}-DDX3Y^{helicae}-DDX3X^{IDR2}	This paper	N/A
pPB DDX3Y^{IDR1}-DDX3X^{helicae}-DDX3Y^{IDR2}	This paper	N/A
pcDNA3 mito-APEX2	This paper	N/A
pPB DDX3X-EGFP	This paper	N/A
pPB DDX3Y-EGFP	This paper	N/A
pcDNA3 FLAG-DDX3X	This paper	N/A
pcDNA3 FLAG-DDX3Y	This paper	N/A
pcDNA3 HA-DDX3X	This paper	N/A
pcDNA3 HA-DDX3Y	This paper	N/A
pET-MCN_His-TEV_V5-DDX3X-mCherry	(Hondele et al., 2019)	N/A
pET-MCN_His-TEV_V5-DDX3Y-mCherry	This paper	N/A
pET-MCN_His-TEV_V5-DDX3X^{IDR1}-DDX3Y^{Helicae}-DDX3Y^{IDR2}-mCherry	This paper	N/A
pET-MCN_His-TEV_V5-DDX3Y^{IDR1}-DDX3X^{Helicae}-DDX3X^{IDR2}-mCherry	This paper	N/A
pET-MCN_His-TEV_V5-DDX3X^{IDR1}-DDX3X^{helicae}-DDX3Y^{IDR2}-mCherry	This paper	N/A
pET-MCN_His-TEV_V5-DDX3Y^{IDR1}-DDX3Y^{helicae}-DDX3X^{IDR2}-mCherry	This paper	N/A
pET-MCN_His-TEV_V5-DDX3X^{IDR1}-DDX3Y^{helicae}-DDX3X^{IDR2}-mCherry	This paper	N/A
pET-MCN_His-TEV_V5-DDX3Y^{IDR1}-DDX3X^{helicae}-DDX3Y^{IDR2}-mCherry	This paper	N/A
pMAL-c2X	(Walker et al., 2010)	Addgene Plasmid #75286, RRID:Addgene_75286
pMAL-c2X-DDX3X	This paper	N/A
pMAL-c2X-DDX3Y	This paper	N/A
pcDNA5/FRT/TO APEX2-GFP	(Padron et al., 2019)	Addgene Plasmid #129640, RRID:Addgene_129640
pJ4M/TDP-43	(Hallegger et al., 2021)	Addgene plasmid #104480, RRID:Addgene_104480

REAGENT or RESOURCE	SOURCE	IDENTIFIER
pPB APEX2-DDX3X	This paper	N/A
pPB APEX2-DDX3Y	This paper	N/A
pPB APEX2-EGFP	This paper	N/A
Software and Algorithms		
HISAT2	(Kim et al., 2015)	https://ccb.jhu.edu/software/hisat2/index.shtml, RRID:SCR_015530
DESeq2	(Love et al., 2014)	https://bioconductor.org/packages/release/bioc/html/DESeq2.html, RRID:SCR_015687
featureCounts	(Liao et al., 2014)	http://bioinf.wehi.edu.au/featureCounts/, RRID:SCR_012919
trimmomatic	(Bolger et al., 2014)	http://www.usadellab.org/cms/index.php?page=trimmomatic, RRID:SCR_011848
R	https://www.r-project.org	https://www.r-project.org, RRID:SCR_000036
Fiji	(Schindelin et al., 2012)	https://imagej.net/Fiji, RRID:SCR_002285
GraphPad Prism	GraphPad Software	https://graphpad.com/scientificsoft, RRID:SCR_002798
Other		
384-well microscopy plates	Brooks Life Sciences	Cat#4ti-0203
Amicon ultra-15	EMD Millipore	Cat# UFC901024